eTransportation 23 (2025) 100392

Contents lists available at ScienceDirect

eTransportation

journal homepage: www.journals.elsevier.com/etransportation

Electric machine co-optimization for EV drive technology development: Integrating Bayesian optimization and nonlinear model predictive control

Christoph Wellmann [a], Abdul Rahman Khaleel [a], Tobias Brinkmann [a], Alexander Wahl [b], Christian Monissen [a], Markus Eisenbarth [a], Jakob Andert [a,*]

[a] Teaching and Research Area Mechatronics in Mobile Propulsion, Faculty of Mechanical Engineering, RWTH Aachen University, Forckenbeckstraße 4, 52074, Aachen, Germany

[b] FEV Europe GmbH, Neuenhofstraße 181, 52078 Aachen, Germany

ARTICLE INFO

Keywords:
Model Predictive Thermal Control
Thermal field weakening
Powertrain right sizing
Electric machine design
Bayesian optimization

ABSTRACT

Electric powertrains are becoming increasingly prevalent in various mobile propulsion applications, not only due to legislations for lower CO_2 emissions and local pollution, but also due to growing sustainable consciousness. However, conceptualizing those systems, consisting of component and controller design processes, is a complex task. The complexity itself arises from the amount of requirements for design objectives and use-cases, which can be met inside a multidimensional parameter space. Additionally, system design and evaluation are inherently tied to coupled component and system control strategy optimization. In this context, the paper presents a fully automated active machine learning methodology applied for a combined optimization of electric machine and system controller design, considering system performance, durability, and energy consumption. During this iterative approach a stochastic optimization of a permanent magnet synchronous machine (PMSM) takes place, constrained from a nonlinear model predictive control in a model-in-the-loop system environment. The active learning is covered by a Bayesian optimization algorithm with a Gaussian process regression to determine the most suitable parameter set in terms of exploration and exploitation. To demonstrate the feasibility of this novel methodology, a thermal subsystem from an electrified state-of-the-art powertrain has been used and further optimized regarding PMSM scaling and final gear ratio. Different real-world drive scenarios from highway to city were taken into account to cover typical sport utility vehicle use-cases. It could be shown that the electric machine losses of the optimized system are reduced by up to 32.7 %, which equals a consumption of $-0.43\ \frac{\mathrm{kWh}}{100\mathrm{km}}$ compared to the reference vehicle. Due to slightly worse operating conditions of the inverter the whole system consumption has been minimized by $-0.35\ \frac{\mathrm{kWh}}{100\mathrm{km}}$. Three parameter studies with fixed iteration count have been executed to find the optimal machine diameter to be increased by 25 % and the length slightly reduced by 16 %. Moreover, the total gear ratio was adjusted by −31 % to shift the load points of highest energy conversion into the machine's optimal efficiency area.

1. Introduction

Electric vehicle (EV) sales have been growing significantly in the past decades, especially since 2018 the EV fleet has increased six times, making a global share of 18% [1,2]. This trend is encouraged by the manufactures focus on electric powertrains, annually increasing the volume of available models by 15% [1]. Considering continuity, a break even point with available internal combustion engine (ICE) models could be reached by the end of this decade [1]. This is supported not only by the superior efficiency advantage of electric systems, but also by a growing clean energy economy [2].

Nevertheless, this is not accounting for all vehicle classes, for example electrified heavy-duty trucks with a global share of 1%, suffering from the competitiveness in the total cost of ownership (TCO) against their ICE counterparts [2]. Moreover, electrified systems rely mostly on critical minerals, like rare earth materials for permanent magnet synchronous machines (PMSM) or lithium for battery production. This demand is rapidly reaching the highest share between renewable energies and grid systems [2]. As a result, the development of electrical systems needs to be continuously optimized, whether for improved battery technologies or increased range, while still addressing sustainability and affordability [3,4]. These challenges and requirements

* Correspondence to: Teaching and Research Area Mechatronics in Mobile Propulsion, RWTH Aachen University, Forckenbeckstraße 4, 52074, Aachen, Germany.
E-mail address: andert@mmp.rwth-aachen.de (J. Andert).

https://doi.org/10.1016/j.etran.2024.100392
Received 9 August 2024; Received in revised form 28 December 2024; Accepted 28 December 2024
Available online 9 January 2025

Nomenclature

Abbreviations

AC	Alternating current
AGS	Active grille shutter
ARD	Automatic relevance determination
AWD	All-wheel drive
BEV	Battery electric vehicle
BO	Bayesian optimization
DC	Direct current
DoE	Design-of-experiment
EGW	Ethylene glycol water
EM	Electric machine
EMS	Energy management strategy
EV	Electric vehicle
FEA	Finite element analysis
GA	Genetic algorithm
GP	Gaussian process
HEV	Hybrid electric vehicle
HEX	Heat exchanger
HV	High voltage
ICCU	Integrated charging control unit
ICE	Internal combustion engine
IGBT	Insulated-Gate-Bipolar-Transistor
LPTN	Lumped parameter thermal network
MiL	Model-in-the-Loop
MPC	Model predictive control
NMPC	Nonlinear model predictive control
NVH	Noise vibration harshness
OCP	Optimal control problem
PMSM	Permanent magnet synchronous machine
RB	Rule-based
RMSE	Root mean square error
RL	Reinforcement learning
RPC	Remote procedure call
RTI	Real time iteration
SUV	Sport utility vehicle
TCO	Total cost of ownership

Greek Symbols

α	Thermal parameter in [−]
η	Efficiency in [%]
θ	Vector of hyperparameters in [−]
σ_f	Variance of the (noise free) signal in [−]
σ_n	Noise variance in [−]
ϕ	Opening proportion of actuator in [−]
μ	Prior mean function of the GP in [−]
ρ	Weighting factor in [−]
χ	Domain of objective function in [−]

Latin Symbols

$\dot{V}$	Volume flow in $\left[\frac{\mathrm{l}}{\mathrm{min}}\right]$
$\mathbf{f}_*$	Gaussian process (posterior) prediction
$\bar{\mathbf{f}}_*$	Gaussian process posterior mean
$\mathbf{p}$	Parameter trajectory
$\mathbf{s}$	Slack variable vector
$\mathbf{u}$	Input/Control vector
$\mathbf{x}$	State vector
$\mathbf{x}_{\mathrm{Design}}$	Vector of design training inputs
$\mathbf{y}_{\mathrm{MPC}}$	Output vector of MPC
$\mathbf{y}$	Observed values resulting from observations at locations $\mathbf{x}_{\mathrm{Design}}$
a	Thermal parameter in [−]
A_{Surf}	Front surface in [m^2]
b	Thermal parameter in [−]
BF	Iron Loss Build Factor in [−]
c_d	Drag coefficient in [−]
d	Dimension in [−]
D	Diameter in [mm]
$\mathscr{D}$	Dataset
$E_{HV,Bat}$	Battery capacity in [kWh]
f_r	Rolling friction coefficient in [−]
H	Height in [mm]
i	Index of samples in [−]
i_{RMS}	Root-Mean-Square of AC current in [A]
$i_{Tot,Rear}$	Gear ratio of the rear drive unit in [−]
I	Unit matrix
J	Cost function in [−]
k	Scaling factor in [−]
K	Covariance matrix
l_m	Characteristic length scale
L	Length in [mm]
m	Maximum modulation index in [−]
$m_{Vehicle}$	Weight of vehicle in [kg]
M	Torque in [N m]
n	Rotational speed in [rpm]
$\mathscr{N}$	Gaussian normal distribution
p	Pole pair number in [−]
P	Power in [W]
r_{dyn}	Dynamic wheel radius in [m]
R	Resistance in [Ω]
t	Time in [s]
T	Temperature in [°C]
U	DC voltage in [V]
W	Width in [mm]
X	Matrix of training inputs
X_*	Matrix of test inputs
z_l	Linear penalization in [−]
Z_l	Quadratic penalization in [−]

necessitate advancements in the design of each new system. To overcome the challenges of suboptimal EV designs, a necessary combination of size and control optimization, using machine learning techniques for faster prediction of system behavior was concluded in [4]. One component of uttermost interest, impacting the on-board energy conversion and accounting for a major loss source during traction operation, is the electric machine (EM) [5]. One way to minimize the loss generation is an electromagnetic right-sizing in combination with a thermal conditioning of the component, which also helps to achieve performance and efficiency requirements. In the past, multiple studies have been executed analyzing and optimizing the EM regarding these challenges, see Table 1.

In general, these can be clustered by their respective optimization layers, applied methods and use-cases. The optimization layers consider thermal system control and component design, as well as a combination of both. For applied methods, either numerical optimization or machine learning techniques have been used. Even a combination of both approaches is applicable to optimize the two different use-cases of a hybrid electric vehicle (HEV) or fully battery electric vehicle (BEV).

Multiple optimization potentials for thermal system control approaches exist, including efficiency, performance, safety and waste heat recovery objectives [6,7]. For example in [8,9] a thermal optimization of the EM has been focused, utilizing the temperature dependency of electrical losses in a model predictive control (MPC) approach. Other contributions shift the objectives from an EM efficiency to an EM performance point of view and extend the MPC control strategy,

Table 1
Publications that consider application optimization potentials by using system control strategies and/or component design enhancements for EMs. The color coding refers to the applied use-cases, namely hybrid electric vehicle (orange), battery electric vehicle (green) and not defined system boundaries (black).

	Optimizing electric vehicles by considering		
	Thermal system control	EM design	Co-design of EM and control
Numerical optimization	[8][9][12][10] [11]	[13]	[14][15][16]
Machine learning	[17][18] [19]	[20][21] [22][23] [24][25] [26]	[27]
Combination of machine learning and numerical optimization	[28][29]	[30]	**This paper** [31]

minimizing track time or maximizing reference tracking by traction torque actuation and thermal derating mitigation [10,11]. As these publications feature a white or gray box system identification and representation, numerical optimization methods were used for system control purposes. For further overviews on thermal system controls for EM temperature conditioning, it is referred to [9].

In order to decrease online computation effort of numerical optimization methods, machine learning derived control strategies with a black-box system character in form of neural nets can be used [19, 32,33]. A predominant example is the energy management strategy (EMS) for BEV using reinforcement learning (RL) in [17] or [18], including powertrain heat dissipation and cabin heating. In both cases the thermal system actuation, which encompasses heating, ventilation, and air conditioning control, such as the compressor and fan speed, was the variable subjected to optimization. In [17], the objective function included energy consumption, battery aging and cabin comfort, but leaving EM operating point affection out of scope as a constant efficiency gain is assumed. The same assumption accounts for [18], where besides the cabin temperature root mean square error (RMSE), power consumption of the positive temperature coefficient heater, fan and compressor is minimized.

In recent publications, a combination of machine learning and MPC techniques for EMS in HEV has been proposed to overcome the inherent weaknesses of each approach, such as the real-time capability of MPC and the costly learning process of RL [28,29]. Therefore, the authors in [28] propose a model-based RL method, learning the optimal control sequence for fuel consumption and state of charge deviation minimization under numerous driving conditions. Herein, the EM efficiency is presented as a function of the operating point, but neither the temperature dependence nor the active influence of controls is modeled. The power split focus of ICE and EM is maintained in [29], combining long short-term memory neural networks for velocity prediction with a fuel consumption MPC, also penalizing gradient controls of each gear and mode switch. Only the work in [29] includes temperature effects, but just from battery component perspective.

Regarding the EM design process, various optimization studies have already been carried out, focusing performance, efficiency, thermal and noise vibration harshness (NVH) objectives [4,34]. In [13], analytically derived powertrain designs are convexified and solved regarding the minimum TCO, yielding global optimality guarantees. To achieve this system simplification, high-level assumptions were made for the EM design, leveraging single component model accuracy. Unfortunately, the trade-off for accuracy inside a multi-objective optimization is typically not following a convex trend, which lacks global optimum potential for gradient-based numerical optimization methods [35].

Therefore, stochastic methods gained significant attentions in past years. Apart from design-of-experiment (DoE) derived surrogate modeling [23] or meta heuristic approaches [21], mainly two different algorithms were used when it comes to machine learning techniques. This includes genetic algorithms (GA) [22,24,25,30] and Bayesian optimization (BO) in [20,26]. Both can be characterized as active learning methodologies, exploring the parameter space for the optimized solution, whereas GA have been found to be more common in EM design for the past decades. These techniques have been applied to a diverse range of machine types. For instance, in [30], they were employed to optimize torque ripple in direct current (DC) machines through rotor teeth geometry adaptation. Herein, a direct search method has been combined with a GA to enhance the convergence of the estimated convex hull. Other examples include efficiency [25] or torque density [22] optimizations of PMSM. In most cases the design space included more than ten continuous or integer parameters. Comparing the simulated candidate designs, in all GA cases far more than 100 iterations have been executed, which adds up to a significant evaluation time for computing time intensive design functions. To overcome challenges with low convergence rates, BO has drawn far more attention in the past years as a probabilistic regression and prediction routine for costly function evaluations [26,36]. In [26], BO algorithm needed much fewer evaluations than GA for the same quality of the results and in [20] a Nissan Leaf EM has been optimized for better efficiency in a worldwide harmonized light vehicles test cycle with less then 100 iterations.

The third optimization column in Table 1 is marked by co-design approaches, accommodating controller and component design/dimension, to achieve a system-level optimum [15]. They can be classified in nested and simultaneous methodologies [37]. Purely gradient-based numerical optimizations allow for simultaneous control and design optimization in case the system model is differentiable and can be discretized over time in the respective use-cases [14–16]. In [16], an energy optimal sizing for a BEV application is targeted, considering maximum EM power, battery capacity and gear ratio as design parameters, motor power and selected gear ratio as control variables. Even though this problem formulation allowed for a comparably infinite prediction horizon, as the cycle is optimized at once, the optimal control problem (OCP) lacks implementation capability due to computational effort. Furthermore, the EM operation is actively tuned by size and gear ratio selection into the most efficient energy conversion area, but thermal effects were left out of scope. The contribution of [14] employs a nearly identical set of control and design variables for TCO optimization, including the dimensioning of thermal management in terms of EM and transmission heat losses. Since the EM was once again represented by convex models, the investigation did not include the nonlinearities, resulting from thermal losses. Another simultaneous co-design publication in [15] focus on the HEV use-case with fuel consumption and capital cost minimization, while maintaining a system robustification regarding design decision variables. While EM scaling and torque control has been optimized, thermal dependencies have not been investigated.

When accounting for global optimality of nonlinear problem formulations, the usage of stochastic models is necessary [15], which could be achieved in a nested optimization manner as implemented in [27,31]. In [27], a GA methodology aims to minimize fuel consumption and emissions by introducing design variables for EM and ICE power as well as control variables of the heuristic control strategy in each gene. While the heuristic strategy is designed around hybrid mode switches, no online optimization is covered, whereas the work in [31] extends the HEV component sizing with online energy management adaption, adjusting proportional integral controller gains regarding optimal EMS. Nevertheless, the control strategy itself is still rule-based.

In conclusion, current EM design processes still lack a comprehensive strategy for optimal thermal system control, including temperature-dependent electromagnetic loss effects. The main contributions of this paper in that research field are as follows:

1. **Integration of Electromagnetic Design and Thermal System Control in EM Development Processes**: This paper addresses a

Table 2
Reference system parameters of the SUV benchmark vehicle with performance values given on EDU output shafts [38].

Parameter	Specification
Dimensions $(L/W/H)$	(4635/1890/1605) mm
Powertrain layout	AWD
Maximum torque $M_{\text{Peak,System}}$	605 N m
Maximum power $P_{\text{Peak,System}}$	225 kW
Battery capacity $E_{\text{HV,Bat}}$	72.6 kWh
Curb weight m_{Vehicle}	2095 kg
Front surface A_{Surf}	2.5 m^2
Rolling friction Coeff. f_r	0.0146 –
Drag Coeff. AGS open $c_{\text{d,open}}$	0.302 –
Drag Coeff. AGS closed $c_{\text{d,close}}$	0.288 –
Dynamic wheel radius r_{dyn}	0.35 m
Gear ratio rear drive $i_{\text{Tot,Rear,Ref}}$	10.65 –

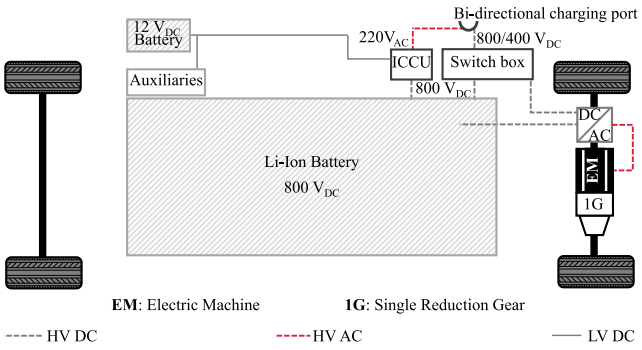

Fig. 1. Electrical and mechanical system architecture of the reduced vehicle system configuration [38,39]. (For interpretation of the references to color in this figure legend, the reader is referred to the web version of this article.)

Table 3
Control parameters for the online system optimization [9].

Parameter	Description
$n_{\text{Pump,EGW}}$	EGW Pump Speed Request in rpm
n_{Fan}	Fan Speed Request in rpm
ϕ_S	AGS Position Request in %
ϕ_{Rad}	Bypass Valve Position Request in %
$n_{\text{Pump,Oil}}$	Oil Pump Speed Request in rpm

critical gap in state-of-the-art EM design processes by introducing a co-optimization methodology to satisfy system objectives, while considering the correlations of component design and optimal thermal control.

2. **Mission-Specific Powertrain Optimization**: The proposed methodology enhances performance capabilities, due to "mission-specific right-sizing" of the powertrain for the designated use-cases, scaling the electromagnetic performance, while ensuring a predictive active temperature conditioning to maximize the peak operation time.
3. **Improved Thermal Efficiency via Machine Learning**: By leveraging machine learning, the paper presents an approach to enhance thermal efficiency related effects by learning the EM heat dissipation and optimally controlling its distribution between the components.

For this reason, the paper starts with the introduction of the reference system and the problem formulation in Section 2, which includes the respective optimization parameters and objective functions. Followed by the detailed representation of the automated design and control derivation of the system in Section 3, the active learning methodology is going to be explained in Section 4. Finally the results of three parameter studies with different multi-design-objective-weightings are investigated in Section 5. Section 6 summarizes the paper and is giving an outlook to future contributions.

2. Problem setup

This section sets up the problem formulation of the contribution. At first, the initial system architecture with its EM parameters and control strategy variables is presented. This sets the baseline for subsequent optimization potential evaluations. Thereafter, the objective functions for control and design are going to be introduced and reformulated into a nested 2-layer optimization framework.

2.1. Vehicle system architecture

The reference vehicle for the derivation of the system model description is an all-wheel drive (AWD) battery electric and state-of-the-art sport utility vehicle (SUV) with a curb weight of 2095 kg and a 800 V boardnet architecture. It achieves a maximum system power of 225 kW and a combined torque of 605 N m on the EDU output shaft, propelled from two PMSMs. As part of a teardown and benchmarking study all component layouts and system data has been available. Table 2 summarizes the most relevant system specifications for this work. It depicts the benchmark vehicle system parameters, which are mainly responsible for the force excitation at the wheel. Noteworthy is the adjustable drag reduction by implementing an active grille shutter (AGS) with its opening ratio ϕ_S, allowing for an online control degree of freedom on the powertrain load points. The drag coefficient with opened AGS $c_{\text{d,open}}$ has been relatively determined with the assumptions from [8]. Over the front and rear gear stages with a total ratio of $i_{\text{Tot,Rear}} = i_{\text{Tot,Front}}$ the traction torque in the AWD vehicle system configuration is transferred from the EM output shafts to the wheel.

For the initial implementation and verification of the co-design approach, the amount of powertrain components and complexity has been reduced, changing the electrical and mechanical architecture to a rear-wheel-drive (RWD) configuration, as depicted in Fig. 1.

The main changes arise from the front electric-drive-unit (EDU) neglection, so that the main powertrain components are the rear PMSM, inverter and gear stages, as well as the integrated charging control unit (ICCU), high voltage (HV) battery and low voltage (LV) thermal auxiliaries. Consequently, the thermal architecture encapsulates this components as shown in Fig. 2.

Hence, the first thermal system loop is the ethylene glycol water (EGW) circuit, using a 50/50 mixture, with the ICCU, rear inverter, the 4-way and 6-way heat exchanger, as well as the radiator as the main heat transferring components [38]. Whereas the ICCU combines the on-board-charging control with the DCDC conversion, the inverter feds the thermally separated located PMSM with a three phase current [38]. The oil circuit is connected via the 4-way heat exchanger (HEX) to the EGW circuit, with its main tasks of lubricating the transmission and cooling the rear PMSM. The PMSM itself has a direct oil cooling concept with a spray cooling ring in front of the end-windings and a cooling bar on top of the outer stator surface applied. Furthermore, the hollow shaft is flooded with oil and equipped with centrifugal nozzles. Due to data availability reasons, the battery and the refrigerant thermal circuit are modeled as system disturbances with constant inlet conditions at the 6-way HEX [38]. Building up upon those available thermal data traces from the benchmarking study, a model identification and validation has been made upfront for the thermally integrated components in Fig. 2. Validation traces for individual components are provided in Figs. A.19 through A.23.

Finally, the system facilitates five control possibilities, one the AGS already mentioned. All the controls are highlighted in Fig. 2 and listed in Table 3.

This includes the two pumps, the fan and the bypass valve to mitigate heat transfer to the environment through the radiator.

For the electromechanical energy conversion the 160 kW rear PMSM is used, incorporating 350 N m of torque, propelled by 4 rotor

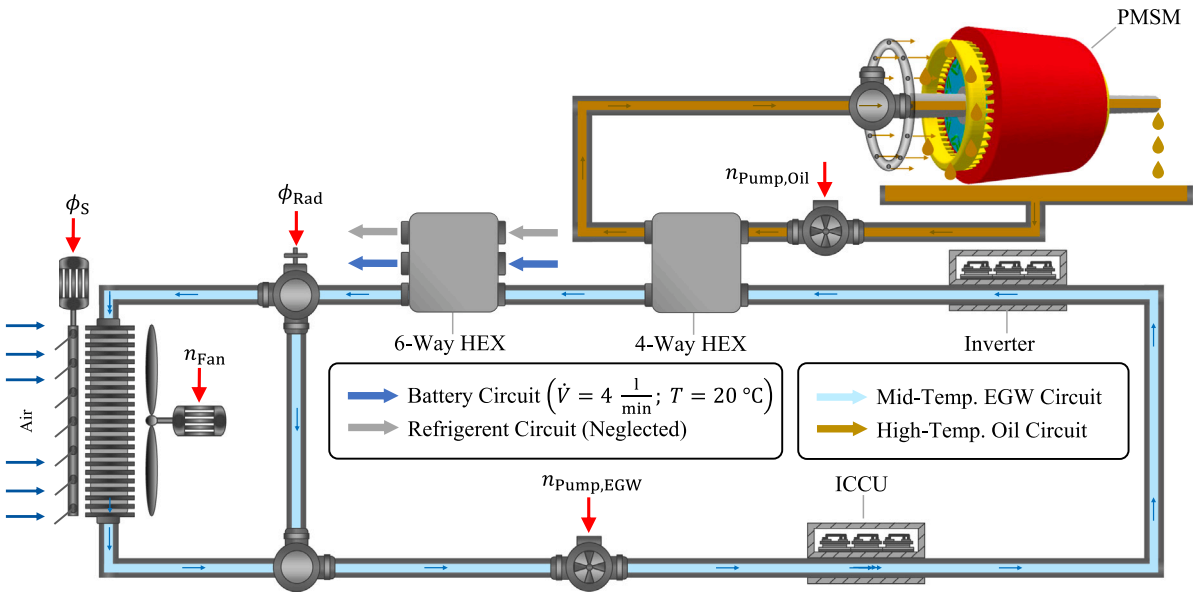

Fig. 2. Mid temperature water–glycol system of the reference vehicle, coupled with the high temperature electric-drive-unit (EDU) oil circuit and constant fluid assumptions for the 6-way linking to the battery and refrigerant loop (System controls are marked with red arrows) [38,39]. (For interpretation of the references to color in this figure legend, the reader is referred to the web version of this article.)

Table 4
Reference parameters of the SUVs rear PMSM [39].

Parameter	Specification
Length $L_{EM,ref}$	238 mm
Diameter $D_{EM,ref}$	200 mm
Pole pair number p	4 –
Number of slots	48 –
Peak torque $M_{Peak,EM,Rear}$	350 N m @ 60 °C
Peak power $P_{Peak,EM,Rear}$	160 kW @ 60 °C and 720 V
Base-speed point	4000 $\frac{1}{min}$ @ 720 V
Magnet array	Two layer interior V
Estimated magnet material	N42UH
Cooling method	Direct oil-cooling

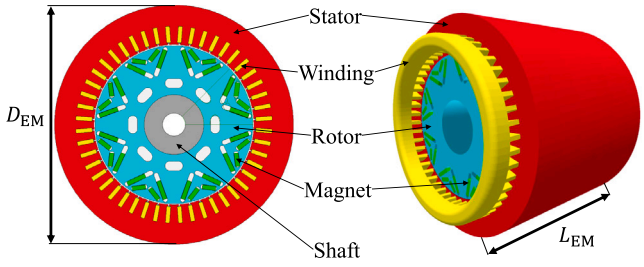

Fig. 3. Cross section and 3D view of reference PMSM model [39,40].

pole pairs and 48 stator slots. All relevant PMSM specifications and cross section views of the reference design are visualized in Table 4 and in Fig. 3, respectively.

In line with the data of Table 4 the PMSM features a double layer interior V magnet array, containing N42UH magnet material [39]. The identification and estimation of the magnet material took part during the teardown and re-engineering of the rear PMSM, regarding the manufacturer performance data [39]. The validated peak torque characteristic of this EM FEA model is given in Fig. A.24.

From the remaining parameters, given in Table 4, the most influential parameters on the electromagnetic energy conversion and performance are the active machine length L_{EM} and diameter D_{EM} [20,41,42]. According to the referenced contributions, they have been selected to open up the design parameter space. As part of the load point determining design parameters, the gear ratio has already been pointed out and is chosen as the third design degree of freedom. All in all, the design parameters $\mathbf{x}_{Design}$ are listed in Table 5 with their respective lower and upper bounds, which align to the packaging constraints [38].

Table 5
Design optimization parameters $\mathbf{x}_{Design}$ for the metamodel creation with their respective upper and lower constraints.

Parameter	Minimum	Maximum
Length L_{EM}	151 mm	300 mm
Diameter D_{EM}	162 mm	250 mm
Gear ratio $i_{Tot,Rear}$	2 –	17.9 –

Besides the upper packaging constraints, also explorations of smaller EMs with numerous gear ratio possibilities shall be emphasized, which is achieved by the boundary scattering around the reference values from Tables 2 and 4.

2.2. Formulation of design and control objectives into multi-layer optimization problem

After definition of the component design and control variables, the objective functions for each of the domains, control and design, need to be defined. To also focus on interaction potentials between those two, both single problems are transferred into optimization layers of a nested co-optimization approach, depicted in Fig. 4.

From system perspective the thermal controls open up the first and innermost layer of the problem formulation. Therewith, the system operation during the use-cases shall be optimized, by minimizing the control objectives, facilitating system output power, temperatures and power losses. A gradient-based numerical solver should be applied based upon past research in that field, due to its handling capabilities of physics informed state–space system models [8,9]. These contributions also include the beneficiary outcomes of a predictive numerical solver deployment in terms of energy consumption minimization. The first layer is superimposed with the system and component design layer, because of its a-priori definition and dimensioning. That includes the already introduced design degrees of freedom inside their specific boundaries in Table 5. Their tuning shall achieve the optimum feedback of the innermost layer. Commonly formulated requirements for BEV in

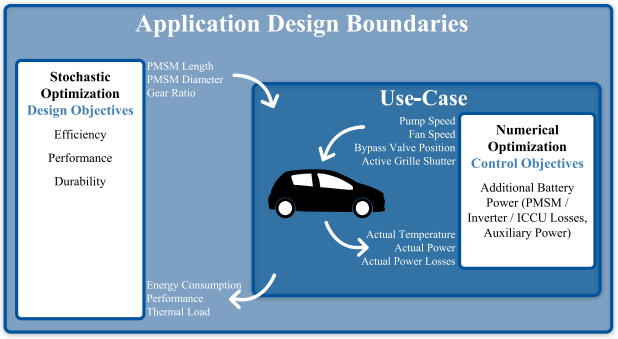

Fig. 4. Nested EM Co-Optimization approach with stochastic and numerical layer.

this layer focus the efficiency, performance, durability, cost, charging and lifetime-assessment of the final system design [43,44]. Hence, energy consumption, performance and thermal load, again minimizing an objective function, have been chosen. For optimization purposes on this upper layer, only a data-driven stochastic method is applicable, because of the non-differentiable inner optimization loop of the controls in the system environment. Due to this restriction and further computational effort requirements on the controller side, a consecutive execution of the two layers has been emphasized.

Looking deeper into the environment of the innermost layer, the use-cases, i.e. the "missions", need consideration, as the system should compromise a good long haul behavior on the highway and facilitate an agile performance in the city. Thus, two real-world use-cases were picked [9]. The city use-case is a cycle around Aachen, encouraging a dynamic start- and stop behavior, as plotted in Fig. 5(a). It is characterized with a maximum and average vehicle velocity of 73.1 kph and 23.1 kph respectively. Additionally, a moderate slope profile has been prevalent. The highway drive in Fig. 5(b) comes at a maximum velocity of 134.2 kph and average speed of 107.68 kph. However, the slope in the pendulum cycle between Aachen and Cologne is flat over large parts.

Both cycles have to be accomplished by the vehicle and will consider the online optimization function J_{Control}, which has been derived in previous publications in [8,9]:

$$\begin{aligned} J_{\text{Control}} = & P_{L,\text{EM}} + P_{L,\text{INV}} + P_{L,\text{ICCU}} + P_{\text{Pump,EGW}} \\ & + P_{\text{Pump,Oil}} + P_{\text{fan}} + P_{\text{Shtr,switch}} - P_{\text{Shtr,Pos}} \end{aligned} \tag{1}$$

The control objective function J_{Control} describes the additional electrical power, besides traction power, for the use-case velocity tracking, considering high-voltage component losses and low-voltage power consumption of the systems thermal actuators. This includes power loss of the EM $P_{\text{L,EM}}$, divided in copper, iron and mechanical loss components, as well as inverter switching and conduction losses, consolidated in $P_{\text{L,INV}}$ [8]. The low voltage power consumption is reflected by the ICCU switching and conduction losses $P_{\text{L,ICCU}}$ and electric power demand of the coolant pumps $P_{\text{Pump,EGW}}$, $P_{\text{Pump,Oil}}$, the fan P_{fan} and the AGS actuator $P_{\text{Shtr,switch}}$. $P_{\text{Shtr,Pos}}$ represents the reduction in wheel power demand due to shutter closure, by reducing the drag coefficient from $c_{\text{d,open}}$ to $c_{\text{d,close}}$.

Besides the control objective for the online system optimization a design objective function needs to be specified. The multi-objective system design function J_{Design}, which is used in this paper, consists of weighted terms for efficiency, performance and durability:

$$\begin{aligned} J_{\text{Design}} = & \underbrace{\rho_{\text{Eff}} \frac{E_{\text{Tot,HV}}}{E_{\text{Tot,HV,0}}}}_{\text{Efficiency-Indicator}} + \underbrace{\rho_{\text{Perf}} \frac{\max(\Delta v_{\text{Ref-Act}})}{\max(\Delta v_{\text{Ref-Act,0}})}}_{\text{Performance-Indicator}} + \\ & \underbrace{\rho_{\text{Dur}} \cdot e^{\max(T_{\text{max,i}} - T_{\text{lim,i}})}}_{\text{Durability-Indicator}} \end{aligned} \tag{2}$$

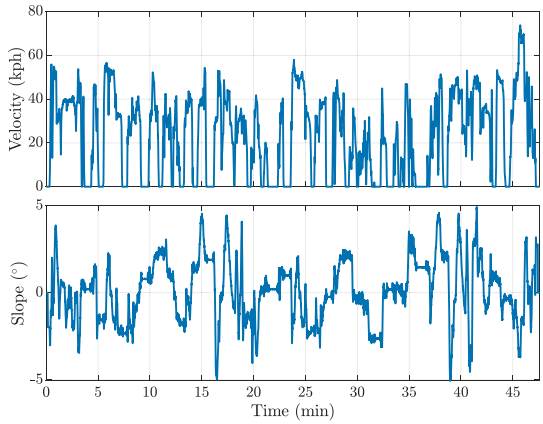

(a) Real world cycle around Aachen to cover city use-case of passenger vehicle car

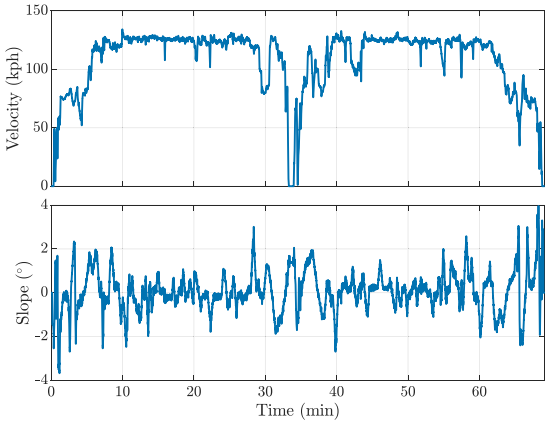

(b) Real world cycle from Aachen to Cologne and back to cover highway use-case of passenger vehicle car

Fig. 5. Primary use-cases for system optimization [9].

The first two objectives of energy consumption $E_{\text{Tot,HV}}$ and performance $\max(\Delta v_{\text{Ref-Act}})$ are normalized based on the particular reference values $E_{\text{Tot,HV,0}}$ and $\max(\Delta v_{\text{Ref-Act,0}})$. Here, energy demand considers the amount of energy being taken from the HV battery between start and end of the two use-cases. The performance criterion evaluates the velocity control deviation, which is inherently combined to the available system output torque. Therefore, the maximum difference to the reference vehicle cycle is calculated and normalized with the initial system behavior. Lastly, the durability objective punishes all temperature limits exceedances exponentially, for example an over-temperature detection of the PMSM, assuming an under-rated system design with instabilities inside the use-cases. After setting up the multi-layer optimization problem for design and control, the underlying iterative methodology will be presented in detail in the upcoming sections.

3. Methodology

As previously pointed out, designing and optimizing systems is a combination of creating suitable component designs and defining proper control strategies for the application. Inevitable both system parts add up to the holistic system behavior. That is why the methodology makes use of the stated nested co-optimization in Fig. 4 and restructures it to a continuous iterative development process. The whole workflow of this framework is depicted in Fig. 6.

Briefly summarized each new parameter set re-scales the geometry of the investigated reference SUV machine. In the next step electromagnetic and thermal simulations of the machine are conducted in

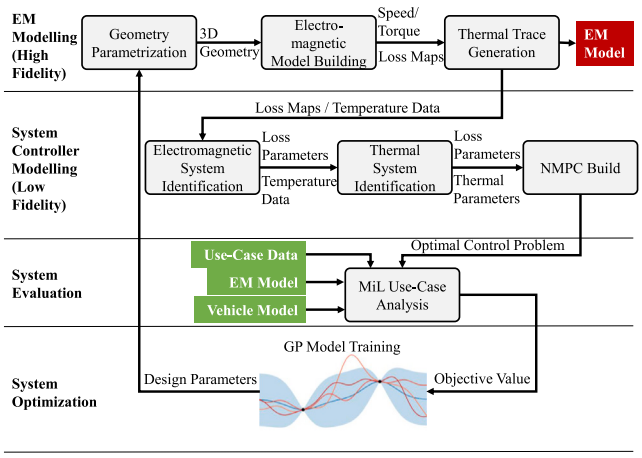

Fig. 6. Iterative machine learning methodology for holistic system optimization of control and hardware design [36].

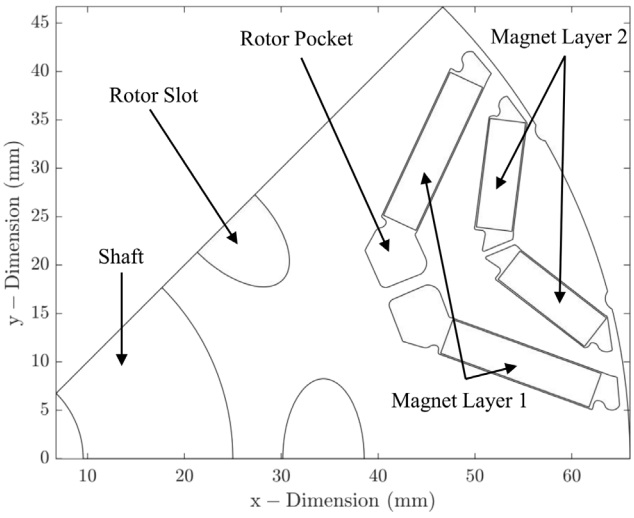

Fig. 7. Custom rotor geometry of re-engineered SUV machine.

ANSYS MOTORCAD® by remote procedure call (RPC) requests from MATLAB® [40]. Using the derived loss maps and thermal traces obtained from the simulation, a low-fidelity model is generated, which will serve as a foundation for the applied nonlinear model predictive control strategy (NMPC). The NMPC predicts future system states and enables an online optimization, minimizing electromagnetic losses and power consumption. Finally, the entire setup of the vehicle is simulated in a model-in-the-loop (MiL) environment, considering the applications specific use-cases to find the scalar objective value. In the following sections, the framework is described in detail.

3.1. Geometry parameter space setup

In the first step the geometric entities of the PMSM are created, using parameters which allow mathematical representation and manipulation of the machine designs. Here, the design process is initiated with the reference vehicle machine. In each following iteration step a new parameter vector leads to a geometrical scaling of the reference machine design.

In fact there are three established scaling methodologies for PMSMs machines, namely axial, radial and rewinding [20,41,42]. This work is focusing the axial and radial scaling as already illustrated in Fig. 3, maintaining small geometrical changes to leave the rewinding unaffected.

The axial scaling procedure modifies lengthwise dimensions of the EM, including stator core length, rotor core length, housing length and overall axial dimensions, using an axial scaling factor $k_{\mathrm{a,i}}$ [41]:

$$k_{\mathrm{a,i}} = \frac{L_{\mathrm{EM,i}}}{L_{\mathrm{EM,ref}}} \tag{3}$$

As shown in Eq. (3) the axial scaling factor is calculated from the motor length quotient of the current machine candidate $L_{\mathrm{EM,i}}$ and the reference machine $L_{\mathrm{EM,ref}}$. The index i assigns for the current iteration step.

For the radial scaling the cross sectional dimensions are altered proportionally, such as the diameter of stator and rotor, as well as the thickness of magnets, air gap and other components. Therefore a radial scaling factor $k_{\mathrm{r,i}}$ is introduced [41]:

$$k_{\mathrm{r,i}} = \frac{D_{\mathrm{EM,i}}}{D_{\mathrm{EM,ref}}} \tag{4}$$

The scaling factor in Eq. (4) describes the relation between the stator lamination diameter $D_{\mathrm{EM,i}}$ of machine candidate i to the reference diameter $D_{\mathrm{EM,ref}}$. During the radial scaling process the relative proportions between components were maintained to ensure a proper alignment between the MOTORCAD geometry and the more detailed custom dxf-rotor-geometry visualized in Fig. 7. The new derived designs set up the finite element analysis (FEA) simulation foundation for the following electromagnetic analysis.

As the initial purpose of this study is centered around setting up and evaluating the multi-system domain methodology, the parameter space is kept small inside this work scope. Nevertheless the generic framework should allow for easy extension of the parameter space in future works.

Table 6
Electromagnetic system constraints for PMSM loss calculation in ANSYS MOTORCAD [45].

Electrical parameter	Value
DC bus voltage U_{Bat}	700 V
Maximum stator current $i_{\mathrm{RMS,Max}}$	240 Arms
Maximum modulation index m	0.95 –
Iron loss build factor BF	1.5 –

3.2. Electromagnetic model building

After geometrical scaling of the machine candidates in ANSYS MOTORCAD, the electrical winding configuration of slot- and end-winding regions is reconsidered to fit the geometry constraints. Hence, the copper slot- and end-winding fill factor is adapted. An electromagnetic description of each PMSM candidate was created using an analysis of the designs over the entire operating envelope, achieved by coupling EMagnetics FEA solvers with thermal modules in ANSYS MOTORCAD. This results in loss maps and peak torque characteristics of the PMSMs, which will be used at later stages in each function iteration. For the electromagnetic system the constraints in Table 6 have been selected.

The DC bus voltage is centered around the average system voltage, while the maximum stator current was taken from the hardware specifications [38]. Maximum modulation index and iron loss build factor were selected from literature, respectively [45,46]. Based on these constraints the loss calculation considers stator, rotor and magnet iron losses, mechanical losses as windage and friction losses, as well as DC and alternating current (AC) copper losses. All loss components are modeled in dependence of the winding and magnet temperature to evaluate system level optimization potential for an active temperature control. For more details regarding the physical loss effects it is referred to [8]. In the end, the loss maps $P_{\mathrm{L,EM}}$ are extracted as a function of speed, torque, winding and magnet temperature:

$$P_{\mathrm{L,EM}} = f(n, M, T_{\mathrm{Wdg}}, T_{\mathrm{Pm}}) \tag{5}$$

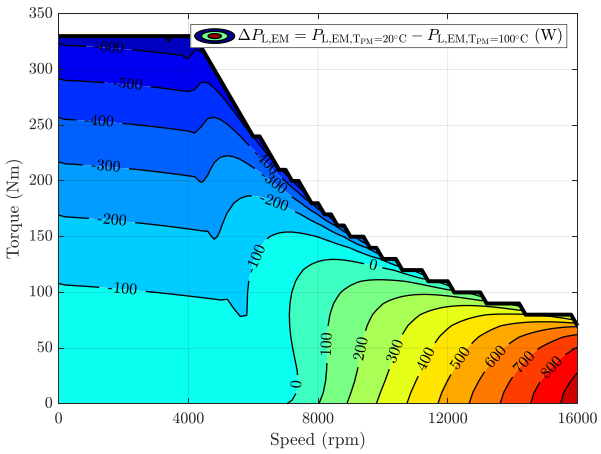

Fig. 8. Differential loss map of reference PMSM at $T_{Wdg} = 20$ °C.

Table 7
Input parameter vector bounds for thermal behavior analysis.

Parameter	Minimum	Maximum
Speed n	0 $\frac{1}{min}$	17 000 $\frac{1}{min}$
Torque M	0 N m	$f(k_a, k_r)$
Volume flow shaft $\dot{V}_{SG}$	0 $\frac{l}{min}$	12 $\frac{l}{min}$
Inlet temperature shaft T_{SG}	0 °C	100 °C
Volume flow spray $\dot{V}_{SC}$	0 $\frac{l}{min}$	12 $\frac{l}{min}$
Inlet temperature spray T_{SC}	0 °C	100 °C
Ambient temperature T_{Amb}	0 °C	40 °C

For temperature set points, two winding temperatures $T_{Wdg} = [20;\ 160]$ °C and four magnet temperatures $T_{Pm} = [-10;\ 20;\ 90;\ 160]$ °C are chosen. The reason for the high discretization of the magnet temperature is to depict the effect of active thermal field weakening. As an example for the mentioned effect, Fig. 8 visualizes the magnet temperature dependency on the losses from the reference SUV PMSM:

While a negative loss difference points out the benefit of a cooler magnet temperature at low speed and high torque operation, a high magnet temperature gets advantageous for the energy conversion at high speeds [12]. Considering such electromagnetic models, active temperature control approaches can result in energy savings at a later stage of the methodology.

3.3. Thermal trace generation

As not only an electromagnetic model of the machine is needed, but also a thermal model for the plant and controller, the high resolution lumped parameter thermal network (LPTN) from ANSYS MOTORCAD is used to identify a transient behavior of the current PMSM candidate. Subsequently, the machine is tested virtually in different driving conditions to understand the thermal flow across the design. As this stage is needed to achieve a model order reduction with subsequent global system identification, four short transient simulations with constant system inputs in a latin hypercube input parameter sampling are taken into account to minimize computation cost. Table 7 summarizes the input dimensions.

While the maximum torque for the thermal analysis depends on the machine scaling k_a and k_r the other input dimensions have fixed bounds based on mechanical system limitations and fluid properties. Hence, each input parameter vector results in an independent thermal excitation and heat transfer, using the specified electromagnetic loss maps from the previous stage and the LPTN of ANSYS MotorCAD.

3.4. Reduced thermal system identification

As the control strategy shall include temperature prediction potentials based upon LPTNs, the trade-off between accuracy and computational cost requires an order reduction of the ANSYS MOTORCAD LPTN. In [9] a model reduction approach for a PMSM has been presented, lumping components in a similar temperature range as a single node. This approach has been adapted to a more general architecture as shown in Fig. 9.

Besides the loss lumping to the winding and magnet region node, the network should facilitate a generic cooling layout character, allowing for different temperature conditioning of stationary and rotating domains. Exemplary for the reference vehicle PMSM its a direct oil cooling, split in end-winding spray and hollow-shaft cooling. Especially for the transient behavior thermal masses are lumped considering the same methodology, while the convective heat transfer between different nodes can be generally modeled by thermal resistances as a function of fluid volume flow $\dot{V}$ and inlet temperature T_{in} [47]:

$$R_{i-j} = R_{th,i-j} \left(\frac{\dot{V}_{ref}}{\dot{V}} \right)^{b_{th} - \alpha_{th}\left(1 - \frac{T_{ref}}{T_{in}}\right)} \left(\frac{T_{ref}}{T_{in}} \right)^{a_{th}} \tag{6}$$

Here R_{i-j} represents the resistance to the heat flow from component i to component j. The factors $b_{th}, \alpha_{th}, a_{th}$ are identified using a global system identification approach by minimizing the error vector between the high fidelity model thermal trace and the low fidelity state space model output [8,48,49]. To maintain a robustness of the identification process to a low amount of sample points, the methodologies in [48,49] have been extended in two ways, whereas the latin hypercube sampling of the model excitation is stage one. But secondly, a global constraint was added to each of the four cycles, to ensure the energy equilibrium is maintained in this non-uniform thermal architecture. This constraint also supports the automatic design process for multiple cooling techniques by penalizing the deviation of possible heat rejection for each cooling flow.

3.5. Reduced electrical system identification

After achieving a thermal simplification of the system for the control strategy, the electromagnetic is transformed into differentiable polynomial equations. The reduced electromagnetic system is modeled, using the curve fitting toolbox in MATLAB [50]. The 4D-loss maps are reduced by polynomial fit of third order as a function of speed and second order as a function of torque, while a linear influence regarding winding and magnet temperature is assumed [9]. For both temperature dependencies sample points at 20 °C and 160 °C are used. Hence, two sets of coefficients coeff_{20} and coeff_{160} are extracted for winding and magnet node losses individually and linearly interpolated during the systems runtime to calculate the current losses $P_{Loss,NMPC}$ as follows [8]:

$$\text{coeff} = \text{coeff}_{20} + \frac{T_{PM} - 20\ °C}{160°C - 20\ °C} \left(\text{coeff}_{160} - \text{coeff}_{20} \right) \tag{7}$$

$$P_{Loss,NMPC} = f(n^3, M^2, T_{Wdg}, \text{coeff}) \tag{8}$$

To ensure integrity throughout the design process, the loss maps are lumped the same way as presented in Section 3.4. For a certain magnet and winding temperature the 2D losses, occurring in the winding node, are compared in Fig. 10.

Although the torque and speed tendencies keep matching quite well between the polynomial output and FEA maps in most operation scenarios, there are still some minor differences. One is the nearly frequency independent winding loss in the base speed range and the other one the changed torque influence on the losses at high frequencies. Nevertheless, it is concluded that throughout a fixation of the polynomial orders in consecutive design iterations, the same trends will occur, allowing for similar and comparable electromagnetic system simplifications in the control strategy.

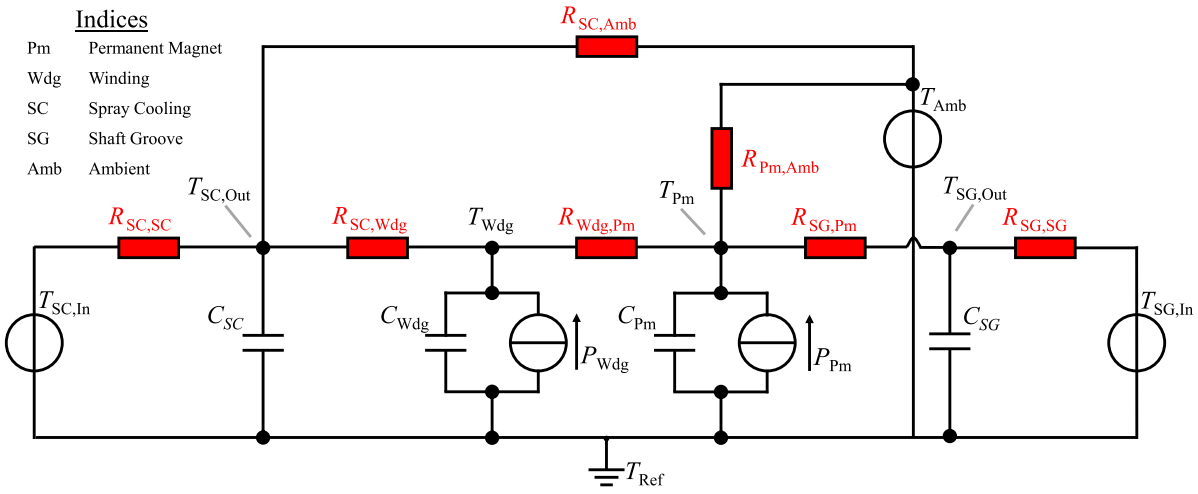

Fig. 9. Generic Lumped-Parameter-Thermal-Network (LPTN) for thermal predictions of a PMSM.

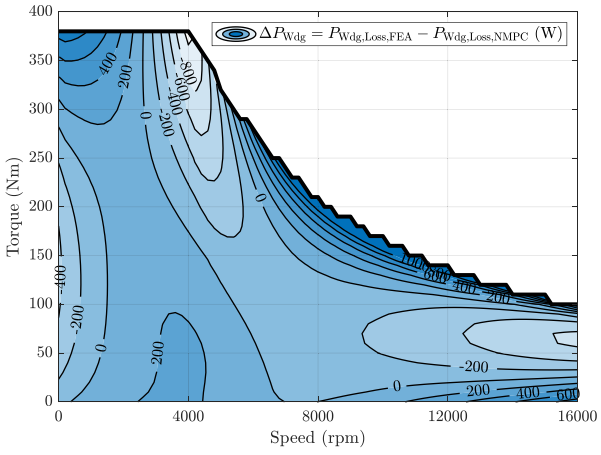

Fig. 10. Exemplary polynomial fitting of losses in winding node.

3.6. Nonlinear model predictive control approach

Nonlinear model predictive control was chosen to ensure an optimization-based, yet modular, adaptive and parameterizable control strategy [51]. Therewith the previously derived component descriptions are combined to a system state–space formulation as presented in [8,9]:

$$\dot{\mathbf{x}} = f(\mathbf{x}, \mathbf{u}, t) \tag{9}$$

$$\begin{bmatrix} 500\ \frac{1}{\min} \\ 0\ \frac{1}{\min} \\ 0\% \\ 0\% \\ 1000\ \frac{1}{\min} \end{bmatrix} \leq \mathbf{u} = \begin{bmatrix} n_{\text{Pump,EGW}} \\ n_{\text{Fan}} \\ \Phi_{\text{Shutter}} \\ \Phi_{2\ \text{W,Valve}} \\ n_{\text{Pump,Oil}} \end{bmatrix} \leq= \begin{bmatrix} 7000\ \frac{1}{\min} \\ 5000\ \frac{1}{\min} \\ 100\% \\ 100\% \\ 7000\ \frac{1}{\min} \end{bmatrix} \tag{10}$$

$$\begin{bmatrix} -40\,^\circ\text{C} \\ -40\,^\circ\text{C} \\ -40\,^\circ\text{C} \\ -40\,^\circ\text{C} \\ -40\,^\circ\text{C} \\ -40\,^\circ\text{C} \\ -40\,^\circ\text{C} \\ -40\,^\circ\text{C} \\ -40\,^\circ\text{C} \\ -40\,^\circ\text{C} \\ -40\,^\circ\text{C} \\ -40\,^\circ\text{C} \end{bmatrix} \leq \mathbf{x} = \begin{bmatrix} T_{\text{Co,RAD}} \\ T_{\text{J,INV}} \\ T_{\text{Co,INV}} \\ T_{\text{W,EM}} \\ T_{\text{Pm,EM}} \\ T_{\text{Co,SC,EM}} \\ T_{\text{Co,SG,EM}} \\ T_{\text{Co,EGW,HEX}} \\ T_{\text{Co,Oil,HEX}} \\ T_{\text{J,ICCU}} \\ T_{\text{Co,ICCU}} \\ T_{\text{Co,4WHEX}} \end{bmatrix} \leq \begin{bmatrix} 100\,^\circ\text{C} \\ 135\,^\circ\text{C} \\ 100\,^\circ\text{C} \\ 155\,^\circ\text{C} \\ 155\,^\circ\text{C} \\ 100\,^\circ\text{C} \\ 100\,^\circ\text{C} \\ 100\,^\circ\text{C} \\ 100\,^\circ\text{C} \\ 100\,^\circ\text{C} \\ 135\,^\circ\text{C} \\ 100\,^\circ\text{C} \\ 100\,^\circ\text{C} \end{bmatrix} \tag{11}$$

$$\mathbf{y}_{\text{MPC}} = \begin{bmatrix} P_{\text{L,EM}} \\ P_{\text{L,INV}} \\ P_{\text{Pump,EGW}} \\ P_{\text{Pump,Oil}} \\ P_{\text{fan}} \\ P_{\text{Shtr,switch}} \\ P_{\text{Shtr,Pos}} \end{bmatrix} = f(\mathbf{x}, \mathbf{u}, n_{\text{Mot}}, M_{\text{Mot}}) \tag{12}$$

where $\dot{x}$ denotes the system state dynamics as a function of the thermal actuator inputs $\mathbf{u}$ and the current system states $\mathbf{x}$ at a given time t. The system states describe different component and coolant temperatures and are bounded by their respective minimum and maximum temperatures. The component temperatures are namely the inverter junction $T_{\text{J,INV}}$, the winding $T_{\text{W,EM}}$, permanent magnet $T_{\text{Pm,EM}}$ and the ICCU junction $T_{\text{J,ICCU}}$ temperature. All the coolant temperatures T_{Co} are modeling downstream temperatures of each component, which are equivalent to the next inlet temperature inline, due to adiabatic and lossless tube simplification [9]. The constraints to the temperature states are set according to the temperature limits and physical limitations of the components. The system controls have already been introduced in Section 2.1 and are depicted in Eq. (10) with their respective limitations. While the position actuators are controlled with continuous percentage requests, the pumps have requirements for a certain idle speed, in case of the EGW pump $n_{\text{Pump,EGW}}$, or minimum speed for lubrication purposes, in case of the oil pump $n_{\text{Pump,oil}}$.

The system's gray-box character allows electrical, thermal and mechanical parameter changes to be quickly compiled and tested in a virtual environment. Therefore the following OCP of the acados-framework for nonlinear programs is being applied [51]:

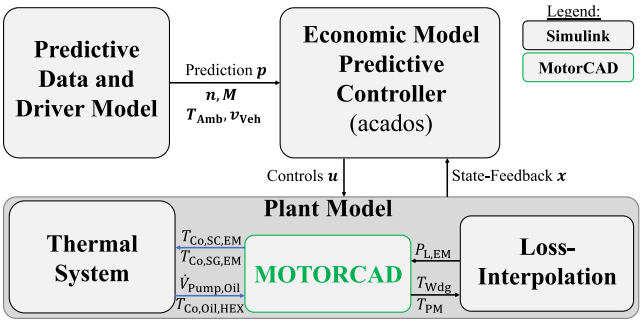

Fig. 11. Scheme of system simulation to derive design objective values [9].

$$\min_{\mathbf{x}(\cdot),\mathbf{u}(\cdot),\mathbf{s}(\cdot)} \int_0^T l(\mathbf{x}(\tau),\mathbf{u}(\tau),\mathbf{p}) + \frac{1}{2}\begin{bmatrix} s_1(\tau) \\ 0 \\ 1 \end{bmatrix}^T \begin{bmatrix} Z_1 & 0 & z_1 \\ 0 & 0 & 0 \\ z_1^T & 0 & 0 \end{bmatrix} \begin{bmatrix} s_1(\tau) \\ 0 \\ 1 \end{bmatrix} d\tau \tag{13}$$

subject to:

$$\dot{\mathbf{x}} = f(\mathbf{x},\mathbf{u},t), \quad \mathbf{x}(0) = \mathbf{x}_0 \tag{14}$$

$$\mathbf{x}_{\min} \leq \mathbf{x} \leq \mathbf{x}_{\max} \tag{15}$$

$$\mathbf{u}_{\min} \leq \mathbf{u} \leq \mathbf{u}_{\max} \tag{16}$$

where l denotes the Lagrange cost term, defining the stage cost depending on the external cost J_{Control} from Eq. (1), as well as external parameters $\mathbf{p}$ (e.g. torque), temperature states $\mathbf{x}$ and thermal actuator control inputs $\mathbf{u}$. Moreover, the Lagrange cost term is extended with a slack variable penalization, introducing soft constraints for the state variables to enhance solver feasibility [51]. In that regards, Z_1 is the quadratic and z_1 the linear penalization. On the one hand, an equal weighting is applied inside the Lagrange cost term to each addend in Eq. (1), due to the same physical representation of power loss and power consumption. On the other hand, the penalization of the slack variables Z_1 and z_1 have been selected in the same order of magnitude as the Lagrange cost term, to ensure a well conditioned OCP. Eqs. (14)–(16) summarize the main system dynamics with its constraints.

During the online phase of the system, the OCP uses future load states over a defined prediction horizon of 600 s to optimize the control trajectory regarding the scalar control objective function presented in Eq. (1). Accordingly, the system state derivative $\dot{\mathbf{x}}$ is integrated by an implicit Runge–Kutta 1st order. Because of the nonlinearity of the system model, the sequential-quadratic programming algorithm in a real-time iteration (RTI) scheme with multiple shooting discretization [51–53] is applied. Each subsequent quadratic problem is then tackled using a high-performance interior point solver [54]. The execution time of the NMPC is herein 1 s, during which new control outputs are send to the actuators.

3.7. System evaluation framework

Once the necessary sections for the system framework are created, the vehicle and its powertrain are simulated in a virtual MiL environment to acquire performance and efficiency information of the current PMSM candidate and powetrain inside the use-case. The comprehensive system framework is adapted from [9] and has been extended to the new system architecture in Fig. 2 inside MATLAB/Simulink, encompassing three key subsystems: predictive data acquisition, NMPC controller, and the high-fidelity plant model (see Fig. 11).

The main system model consists of two internal loops and one external loop. The internal loops are centering the co-simulation between the high fidelity thermal EM model and the residual thermal system [9].

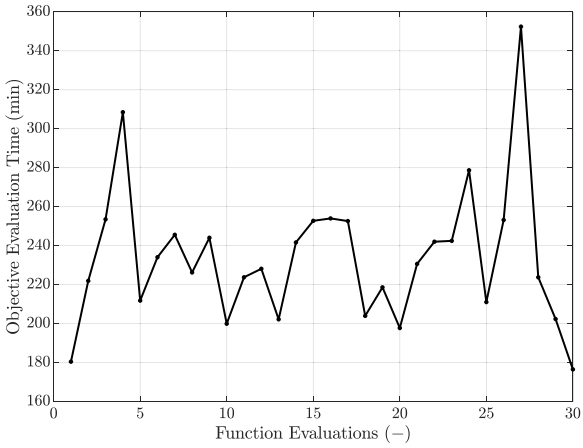

Fig. 12. Design function evaluation trace over 30 consecutive iterations.

Therefore ANSYS MOTORCAD is interfaced by RPCs to facilitate interaction within the plant model regarding thermal inlet conditions as well as heat sources [40]. The heat injection is interpolated with the derived loss maps from an earlier stage in Eq. (5), using the latest known winding and permanent magnet temperatures.

Meanwhile, the external loop describes the control strategy of the system. On the one hand, it requires the state feedbacks, including all observed temperature states for initialization purposes of the OCP in Eq. (14). On the other hand, it needs the cycle data of the use-case for a forward driver model to project the future load points into a parameter trajectory $\mathbf{p}$, which is as well an input to the OCP in the Lagrange objective term in Eq. (13) [9]. Based on this, the NMPC minimizes the cost function by calculating the optimal control sequence and passes its first entry to the plant model.

The residual plant model with its thermal system is mainly based upon [8] and has been extended with parameter sets from available benchmark data of the reference vehicle (SUV) to the new architecture. Thus, the electrical and thermal model of the inverter and ICCU are built upon the available benchmark measurements mentioned in Section 2.1, using the curve fitting toolbox and global system identification techniques for LPTN networks [8,50,55]. The actuators as pumps, fans and the active grill shutter use polynomial equations derived from [8,9] adapted to the new system layout and available parameter sets. Radiator and HEX are modeled by using the ϵ-NTU Theorem for crossflow HEX [8,56,57].

Throughout the use case analysis, the energy demand and the speed offset to the reference and thermal safety margins are tracked to sum the weighted design target value from Eq. (2).

4. Surrogate modeling using Bayesian optimization

To efficiently cover the multi-dimensional parameter space, an active learning approach was chosen, to minimize the computation time until an optimized solution is reached [26]. The training includes the design degrees of freedom, listed in Table 5 and their respective singular design objective values. Highlighting the expansive design evaluation process the turnaround times for single iterations are visualized in Fig. 12.

The data in Fig. 12 has been acquired on a 10-Core 12th Gen Intel(R) Core(TM) i7-1255U with 16 GB of RAM available, without parallelization applied. For this parameter study the turnaround time reaches 352 min peak, and 243 min average which makes the utilization of DoE methods not manageable. Consequently, for this problem setup BO has been selected as a suitable algorithm to cover the exploration–exploitation trade-off with a minimum amount of iterations [20,26].

Besides the system's nested OCP, BO is applied in the second optimization layer generally defined as [26,36]:

$$\mathbf{x}^*_{\text{Design}} \in \underset{\mathbf{x}_{\text{Design}} \in \chi}{\arg\min}\ J_{\text{Design}}(\mathbf{x}_{\text{Design}}) \tag{17}$$

The goal of the algorithm is to find a parameter vector $\mathbf{x}^*_{\text{Design}}$ within the domain χ; $J_{\text{Design}} : \chi \rightarrow \mathbb{R}$ that holds the minimum of the objective function J^*_{Design}. For this, a sequential approach is applied during BO, that is executed with a fixed amount of iterations as termination condition. The outline of the methodology is shown in the Algorithm 1 [36,58]

Algorithm 1 Bayesian Optimization for Design Tuning

Input: Initial dataset $\mathscr{D} = \{(\mathbf{x}_{\text{Design},0}, \mathbf{J}_{\text{Design},0})\}$
1 **repeat**
2 $\quad \mathbf{x}_{\text{Design}} \leftarrow \text{POLICY}(\mathscr{D})$
3 $\quad J_{\text{Design}} \leftarrow \text{OBSERVE}(\mathbf{x}_{\text{Design}})$
4 $\quad \mathscr{D} \leftarrow \mathscr{D} \cup \{(\mathbf{x}_{\text{Design}}, J_{\text{Design}})\}$
5 **until** maximum number of iterations;
6 **return** $\mathscr{D}$

At first an input is defined, which initializes the algorithm with a certain dataset of a design parameter $\mathbf{x}_{\text{Design},0}$ and objective value $\mathbf{J}_{\text{Design},0}$ trace. This also enables a continuation of the optimization process for previously terminated studies. In the end the returned dataset holds the initial and new design data evaluations from the iterative process.

The main iterative process is divided into three tasks, executed until the maximum number of iterations is reached. In this study, this parameter is set to 30. In the beginning a regression model is trained from dataset $\mathscr{D}$ in line 2, being used to derive an optimized parameter vector $\mathbf{x}_{\text{Design}}$ given a certain objective function. Subsequently the observation task in algorithm 1 line 3 is called, which has already been discussed in detail in Section 3. It mainly holds the call of the design function with the new parameter set $\mathbf{x}_{\text{Design}}$. After the new data is acquired the dataset $\mathscr{D}$ is extended to a new dataset.

Typically, Gaussian processes (GP) are used in a BO regression routine as they represent a closed form of modeling predictions and uncertainties in multivariate Gaussian distributions [26,36,59,60]. In particular, this means the objective is modeled as a distribution on functions inside the parameter space $f_{\text{Design}}(\mathbf{x}_{\text{Design}})$. Therein, the modeling of uncertainties is crucial to the application of a BO algorithm, for balancing the adaptive trade-off between exploration (sampling areas with high variance) and exploitation (sampling areas with low predictive mean value), which is one of the major characteristics in an active learning algorithm. For a basic overview on GP's it is referred to [61]. In the beginning of algorithm 1 a prior distribution of the GP is defined, which is separated into a mean $\mu : \chi \rightarrow \mathbb{R}$ and positive definite covariance function $K : \chi \times \chi \rightarrow \mathbb{R}$ [60,61]:

$$\mu(\mathbf{x}_{\text{Design}}) := \mathbb{E}[f_{\text{Design}}(\mathbf{x}_{\text{Design}})], \tag{18}$$

$$K(\mathbf{x}_{\text{Design}}, \mathbf{x}'_{\text{Design}}) := \mathbb{E}[(f_{\text{Design}}(\mathbf{x}_{\text{Design}}) - \mu(\mathbf{x}_{\text{Design}})) \cdot (f_{\text{Design}}(\mathbf{x}'_{\text{Design}}) - \mu(\mathbf{x}'_{\text{Design}}))] \tag{19}$$

While the mean value $\mu(\mathbf{x}_{\text{Design}})$ holds the expected design objective value $\mathbb{E}[f_{\text{Design}}(\mathbf{x}_{\text{Design}})]$ at a certain point x_{Design} in the parameter space, the covariance function $K(\mathbf{x}_{\text{Design}}, \mathbf{x}'_{\text{Design}})$ portrays the correlation of two different parameter locations x_{Design} and x'_{Design}. As the covariance is intrinsic to the chosen kernel function, the available system design data has been taken into account for the choice of an appropriate kernel function. For that reason a non periodic, rather exponential behavior is favored. As the selected optimization parameters yield difference influence on the objective value an automatic relevance determination (ARD) Matern 5/2 kernel has been selected [60]:

$$K(\mathbf{x}, \mathbf{x}'|\theta) = \sigma_f^2(1 + \sqrt{5}r + \frac{5}{3}r^2)\exp(-\sqrt{5}r)$$
$$\text{with}: \ r = \sqrt{\sum_{m=1}^{d} \frac{(x_m - x'_m)^2}{l_m^2}} \tag{20}$$

The hyperparameters θ of this kernel can be expressed as $\theta = \{\sigma_f, l_1, l_2, \ldots, l_m\}$, where σ_f denotes the variance and l_m represents the characteristic length scale in the mth dimension of the kernel [60]. During the model regression after a new parameter observation, these are updated, maximizing the marginal likelihood of the GP [60,61].

After selecting the kernel and gathering the first observation data the posterior distribution of the GP is fitted, based upon the general GP assumption that discretized data from the prior and training data are jointly distributed [26,36,61]. Due to missing prior knowledge of the system's behavior in the selected use-cases, the mean functions of the GP prior are set to zero:

$$\begin{bmatrix}\mathbf{y}\\ \mathbf{f}_*\end{bmatrix} \sim \mathcal{N}\left(\mathbf{0}, \begin{bmatrix}K(X,X) + \sigma_n^2 I & K(X,X_*)\\ K(X_*,X) & K(X_*,X_*)\end{bmatrix}\right) \tag{21}$$

In Eq. (21) X and X_* denote the training/observation and test inputs, with their respective outputs $\mathbf{y}$ and $\mathbf{f}_*$. As the multi-stage design process is assumed to be not deterministic, a noise variance σ_n^2 has been added to the training data covariance $K(X,X)$, whereas the other matrices describe the covariance between training and test inputs $K(X,X_*)$ and its transpose $K(X_*,X)$, as well as between test inputs $K(X_*,X_*)$.

For system predictions and the application of an optimization policy routine the GP posterior is derived by conditioning the joint distribution [36,61]:

$$\bar{\mathbf{f}}_* = K(X_*,X)[K(X,X) + \sigma_n^2 I]^{-1}\mathbf{y}, \tag{22}$$

$$\text{cov}(\mathbf{f}_*) = K(X_*,X_*) - K(X_*,X)[K(X,X) + \sigma_n^2 I]^{-1}K(X,X_*) \tag{23}$$

Eqs. (22) and (23) yield the trained GP with posterior mean $\bar{\mathbf{f}}_*$ and the covariance $\text{cov}(\mathbf{f}_*)$, which are being updated sequentially in algorithm 1 line 2 during the application of the policy.

Consequently, the GP is used for model predictions in every iteration number greater than 1 in the policy to actively determine the next parameter set of length, diameter and gear ratio. The policy, i.e. the acquisition function, determines the search behavior of the BO. This is done by quantifying and optimizing the exploration–exploitation trade-off. In this contribution the commonly used acquisition function "expected-improvement", which evaluates the marginal gain of utility, has been selected [36,58,62]:

$$EI(\mathbf{x}, \mathbf{f}_*) = \mathbb{E}_{\mathbf{f}_*}[\max(0, \bar{\mathbf{f}}_*(\mathbf{x}_{\text{best}}) - f(\mathbf{x}))] \tag{24}$$

To maximize the acquisition function the posterior GP mean is firstly sampled several times to approximate the lowest feasible mean inside the parameter bounds $\bar{\mathbf{f}}_*(\mathbf{x}_{\text{best}})$ [58]. Secondly the posterior GP $f(\mathbf{x})$ is sampled several more times over $\mathbf{x}$ and the resulting expected improvement is evaluated with Eq. (24) [58]. This includes the sparse confidence at earlier iterations, leading to a higher amount of exploring parameter choices. The parameter set x that is maximizing the expected improvement value is finally selected as the new observation parameter set and closing the BO loop.

5. Results

In this section the results of three parameter studies for different design objective weightings in the combined city and highway use-case shall be discussed. Specifically, the effect on the performance and efficiency objective, as well as the coordination of the control strategy adaption to the optimized design will be focused. Table 8 summarizes

Table 8
System energy consumption reduction and performance increase for optimized EM design with thermal NMPC at three different design objective weightings

Efficiency : Performance weighting	1:1	1:0.01	1:0
Energy consumption compared to reference system with RB control (32.79 $\frac{\text{kWh}}{100\ \text{km}}$)	+0.08 $\frac{\text{kWh}}{100\ \text{km}}$ (+0.32%)	−0.18 $\frac{\text{kWh}}{100\ \text{km}}$ (−0.78%)	−0.35 $\frac{\text{kWh}}{100\ \text{km}}$ (−1.52%)
Energy consumption compared to reference system with NMPC control	+0.1 $\frac{\text{kWh}}{100\ \text{km}}$ (+0.43 %)	−0.16 $\frac{\text{kWh}}{100\ \text{km}}$ (−0.67%)	−0.33 $\frac{\text{kWh}}{100\ \text{km}}$ (−1.42%)
Energy consumption compared to optimized system with RB control	−0.026 $\frac{\text{kWh}}{100\ \text{km}}$ (−0.11%)	−0.028 $\frac{\text{kWh}}{100\ \text{km}}$ (−0.12%)	−0.021 $\frac{\text{kWh}}{100\ \text{km}}$ (−0.09%)
Performance	+19.62%	+12.94%	−353.52%
Ref. Parameters [L [mm]; D[mm]; i_{Tot}[−]]	[238; 200; 10.65]	[238; 200; 10.65]	[238; 200; 10.65]
Opt. Parameters [L [mm]; D[mm]; i_{Tot}[−]]	[198.9; 250; 10.73]	[197.6; 225.79; 10.36]	[200.3; 249.3; 7.32]

the performance and efficiency gains of the design and control optimized systems. They are evaluated against the reference system with a NMPC approach, as well as a re-engineered rule-based (RB) control application of the reference and optimized system design. Furthermore, it facilitates the optimized design parameters for length, diameter and final gear ratio. The multi-stage control architecture of the RB approach has been previously published in [8] and was calibrated, considering the benchmark vehicles behavior [38,39] (see Fig. B.26).

Generally there is a clear impact of the three weighting factors ρ_{Eff}, ρ_{Perf} and ρ_{Dur} on the final design recognizable, when comparing the optimized parameter vectors. Due to the normalization of each indicator in Eq. (2), an equal weighting has been applied at first. However, after analyzing the first results, a difference of two orders of magnitude has been observed between the efficiency and performance indicator. For that reason, a weighting of 1:0.01 has been selected to enlarge the possible improvements in the BO routine for efficiency gains. At last, the third parameter study should reveal the maximum capabilities in terms of energy consumption reduction, where performance is of lower matter for the end-customer. Ultimately, these indicator weightings shall be chosen with respect of the certain system application during the concept study phase, depending on key buying factors of end-customers, company philosophies or policy regulations. Differentiating the results of these three studies, the length of the machine is reduced in every scenario, while the diameter is found to be increased to minimize the objective J_{Design} (see Eq. (2)). An exception applies for the final gear ratio, which stays nearly constant as long as the performance objective is included inside the BO routine (see Fig. B.25).

By comparing the two design objectives it is noticeable, that the performance criterion is more sensitive against parameter changes than the efficiency. While the energy consumption spreads around 2% the performance objective differentiates around 373%. Evaluating the energy consumption reduction, a clear deviation between design and control dependency is recognizable. Hence, the EM design of the second and third parameter study accounts for roughly 85%, respectively 94%, of the energy savings. Compared to prior studies utilizing a thermal NMPC approach as described in [9], the minimization of energy consumption relative to the baseline strategy is less pronounced. On the one hand, it is due to the wider EM dimensions and less heat losses, that would allow for a more transient heating and cooling behavior. On the other hand, the use-case selection in this work is not sufficient to realize a high power demand on the system. Future contributions need to take a durability cycle with higher wheel power and ambient temperatures into account, as well as a NMPC adjustment to different cooling topologies with individual cooling actuation, extending the control space and nonlinearities. Nevertheless, the NMPC consistently outperforms the RB approach by up to −0.11%, even in the first study, where the design falls short of realizing an energy consumption reduction. The following subsections should allow for a more in-depth analysis of the values and their fundamental background.

5.1. Optimized EM characteristics

Every adaption of the reference machine is leading inherently to a change in the EM characteristics. This includes new performance ratings as well as energy conversion efficiencies in the selected use-cases. Fig. 13 visualizes the maximum performance changes and the shifted energy conversion heat maps, which were generated by binning speed and torque into 50 bins, followed by additional smoothing.

Only the first and fourth quadrant for powering and recuperation are shown, with speed on the x-axis and torque output on the y-axis. The solid and dashed envelope lines characterize the maximum torque output of the optimized machine and the reference machine, respectively, at a machine temperature of 20 °C and a constant maximum current. Inside the envelope the isolines for the total machine losses are drawn.

At first the attention shall be paid to Figs. 13(a) and 13(b). Both of these optimized systems have been driving the use-cases with a similar final gear ratio, resulting in a nearly identical location of the energy conversion map and the operating points. Moreover, both machines are of almost identical length, but as the second design diameter is slightly smaller, the flux guiding area and magnetic flux density is lower, keeping the same electrical input parameters, which arises in a reduced peak torque capability and higher base speed point. This also shifts regions with the same amount of frequency dependent iron losses to higher speeds, stretching the total loss map to a reduction of up to 50% in the use-cases [8,63]. Predominant is the effect especially for the highway use-case and will lower the heat injection into the reference vehicle's system, see Section 5.3. Considering the performance gain, both design changes allow for an increased acceleration capability in the field weakening area of the machine, underlined by the operation points above the dashed envelope torque line. This effects the performance objective drastically, as the vehicle can follow the velocity trajectory more closely, driven by a vehicle with much lower weight and just slightly lower power capabilities.

Coming to the third parameter study, the machine dimensions are found nearly identical to study one, except for a slight increase in length. For that reason, there is also no major difference in the peak-torque characteristics. The major difference is the $\Delta i_{\text{Tot}} = -31.3\%$ lower gear ratio, shifting the operation points and energy conversions at a constant power into lower speed and higher torque areas, where the lowest energy losses in terms of the scaled reference PMSM occur. Hence, the whole system consumption in the two use-cases could be decreased by −0.35 $\frac{\text{kWh}}{100\ \text{km}}$. Again, the major consumption influence is recognizable for the highway use-case, while the city use-case now suffers from decreased wheel torque capabilities. That is noticeable in the drastically changed performance objective to −353.52% and the yellow areas around the peak torque in the base speed region. Consequently, the vehicle is not capable of following the dynamic standstill accelerations. Nevertheless, the average velocity deviation with 0.05 $\frac{\text{m}}{\text{s}}$ is just slightly affected. For a further analysis on these system trends, it is referred to Section 5.5.

5.2. City use-case controls

In this subsection the control strategy adaption in the city use-case is analyzed. For this, the five different controls and four EM temperatures are depicted in Fig. 14.

Overall no cooling demand or investment in heat shifting for active temperature control is detectable, leaving the pumps and fans at minimum speed. Just for the third optimized system in Fig. 14(c) little actuation of the EGW pump during high acceleration and deceleration phases occurs, leveraging the temperature rise of the inverter

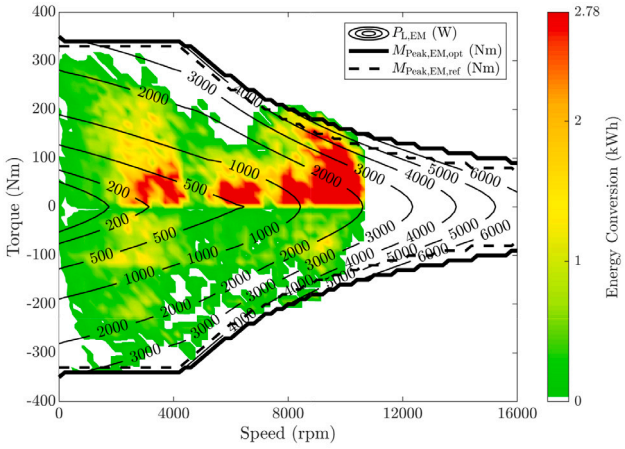

(a) Mission-specific right sized PMSM for efficiency/performance rating of 1:1

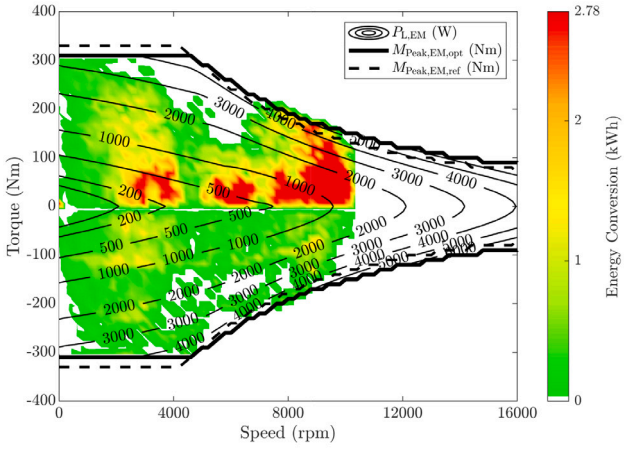

(b) Mission-specific right sized PMSM for efficiency/performance rating of 1:0.01

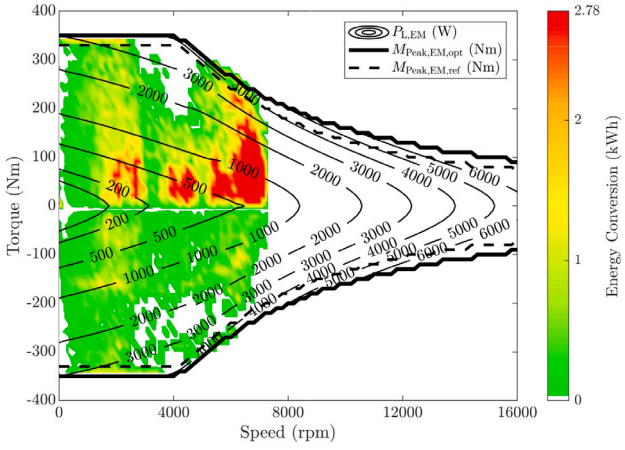

(c) Mission-specific right sized PMSM for efficiency/performance rating of 1:0

Fig. 13. Energy conversion of the analyzed use-cases in PMSM loss map. (For interpretation of the references to color in this figure legend, the reader is referred to the web version of this article.)

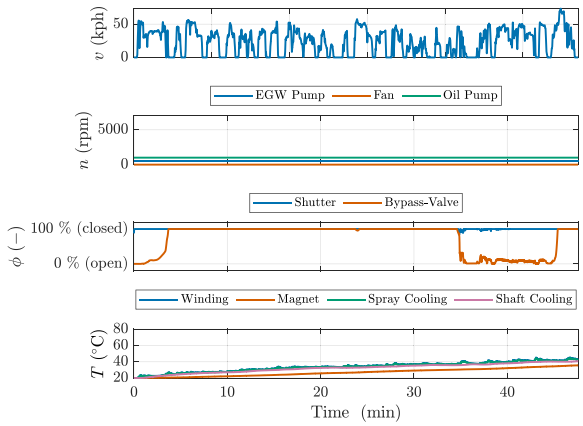

(a) System controls and PMSM temperatures for efficiency/performance rating of 1:1

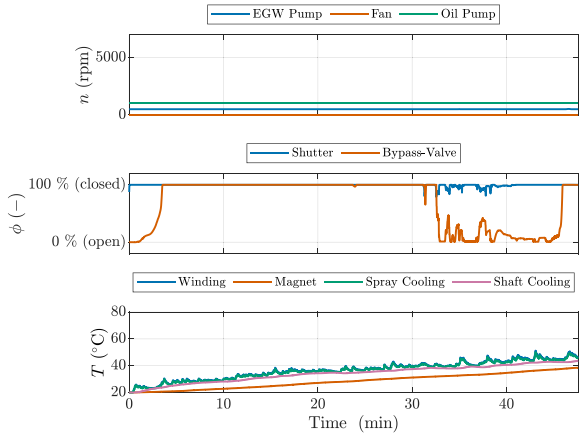

(b) System controls and PMSM temperatures for efficiency/performance rating of 1:0.01

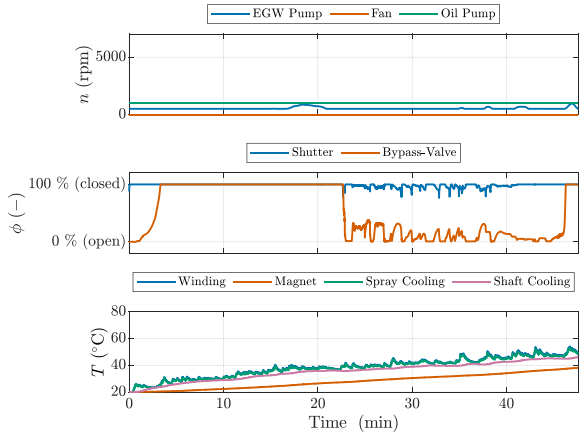

(c) System controls and PMSM temperatures for efficiency/performance rating of 1:0

Fig. 14. Transient system controls in city use-case at T_{Amb} = 20 °C.

junction temperature. For the temperature-dependent loss effects of an Insulated-Gate-Bipolar-Transistor (IGBT) module the reader is referred to [8,64]. Condensed the conduction losses increase proportionally to temperature and higher current demands, arising from a high torque request in acceleration and deceleration phases.

The temperature-dependent conduction losses outweigh the control strategy behavior of the city use-case, as can be seen in the subplots of the active grille shutter and bypass control, as well as the EM temperatures (see Fig. B.27). It should be noted, that due to the low heat losses in the city use-case the spray cooling outlet and winding temperature the graphs are on top of each other. Here, the overall EM temperatures can be considered almost redundant in every optimized system design, as the total amount of EM losses inside the system are

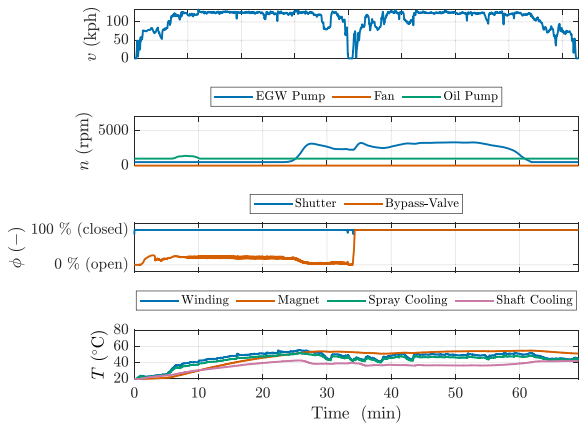

(a) System controls and PMSM temperatures for efficiency/performance rating of 1:1

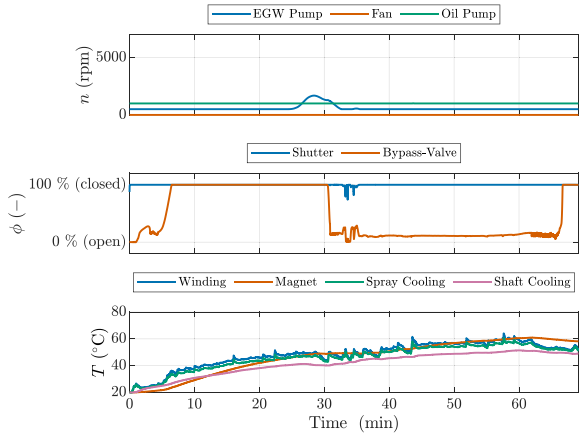

(b) System controls and PMSM temperatures for efficiency/performance rating of 1:0.01

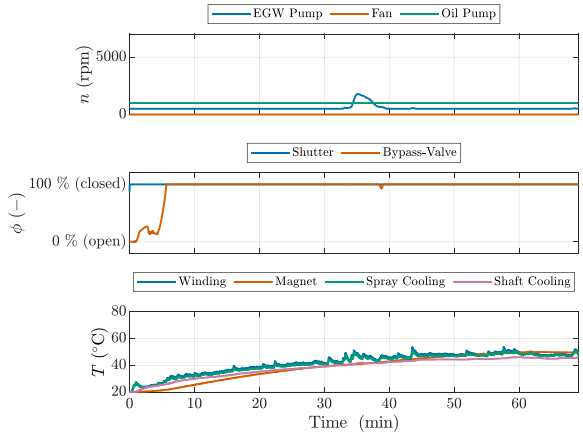

(c) System controls and PMSM temperatures for efficiency/performance rating of 1:0

Fig. 15. Transient system controls in highway use-case at $T_{\text{Amb}} = 20\,°\text{C}$.

rather low and not differ greatly from each other. The potential for an active EM temperature control is therewith marginal. But as the load point is shifting due to the gear ratio decrease from first to third parameter study, the effective current of the IGBT modules increases and subsequently the losses. To achieve a reduction of the losses the NMPC opens the shutter and bypass to achieve earlier cooling. The actuation strategy is here chosen under a trade off between cooling under beneficial circumstances, while maintaining maximum possible heat inside the system. All in all, the automatic adaption of the control strategy to the new system designs showed a plausible behavior, maximizing the systems potential.

5.3. Highway use-case controls

Next is the highway use-case, which is maintaining a high EM speed with intermediate acceleration and deceleration phases. First up, Section 5.1 already revealed that the EM losses are two to three times higher compared to the city driving scenario. Moreover, it has been stated before, that the machine losses are continuously reduced from parameter study one to three. Fig. 15 is capturing the NMPC control behavior and EM temperature increase.

At first the attention should be payed to the speed control of pumps and fan. It stands out, that an increase in system efficiency, especially the EM, leads to less optimization potential for the NMPC to achieve further power consumption reduction. That being said, the advantage to invest in active temperature control to achieve a hot magnet temperature and a cool winding temperature is leveraged with an already better energy conversion in the driven operating points.

For all three system designs the NMPC tries to maintain a closed active grille shutter to mitigate higher air drag, especially because it is not needed for higher cooling demands. The heat transfer over the radiator due to the air leakage volume flow seems to be sufficient to achieve a component temperature control.

The system design one with less efficiency objective optimization is at most trying to lever this drawback with a fast EM temperature heat up, for the usage of active thermal field weakening [9]. Before the deceleration and acceleration phase in the middle of the highway cycle the NMPC ramps up the EGW pump speed and closing the bypass to achieve a higher heat extraction of the oil circuit. Thereby the dominating temperature proportional winding losses are minimized, while the magnet temperatures is nearly unaffected due to a higher thermal resistance to the heat sink.

In the second and third system design the shifted load points increase the inverter conduction losses, which are temperature contradictory to the beneficial higher magnet temperature (see Fig. B.28). Thus, the control strategy adapts to close the bypass early, reducing the EM temperature increase rate, which is lower after all due to the higher efficiency. Additionally, it is limiting the rise of the inverter temperature, being more beneficial for the temperature proportional inverter conduction losses. This holds for the complete cycle with design three. However, in the second design highway use-case, the bypass valve is opened again before the standstill phase and kept open throughout the second phase. This is because the magnet temperature reached a higher level, compared to design three and the NMPC control strategy evaluates energy consumption benefits over the next 10 min by maintaining heat inside the system for the upcoming high speed section, to make use of active thermal field weakening. In the end it yields a higher energy consumption improvement by EM loss reduction due to a magnet temperature increase, compared to the disadvantages on the inverter side at higher temperature.

5.4. System efficiency evaluation

For a detailed system efficiency evaluation the optimized systems are compared against their reference with a RB control approach. The influence on HV system efficiency is evaluated referring to [9]. Fig. 16 sets the component-wise efficiency changes in contrast. While the main analysis from controls and EM characteristics in the use-cases has been made in the previous sections, the efficiency changes shall align and verify these observations.

The actuator power consumption make up for the lowest impact on the system efficiency increase. Minor differences arise from the lesser pump actuation of system two and three, and the slightly higher amount of shutter opening in the city use-case of system three. To

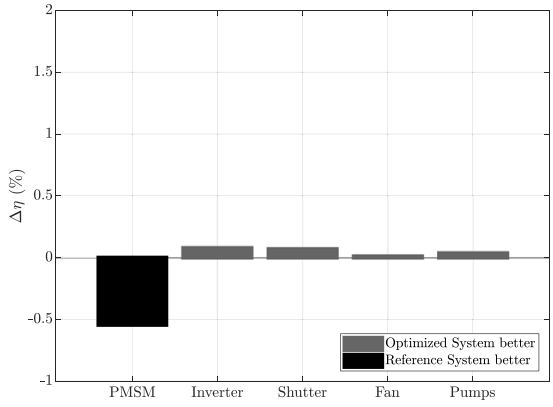

(a) Energy consumption impact of traction and actuator components for efficiency/performance rating of 1:1

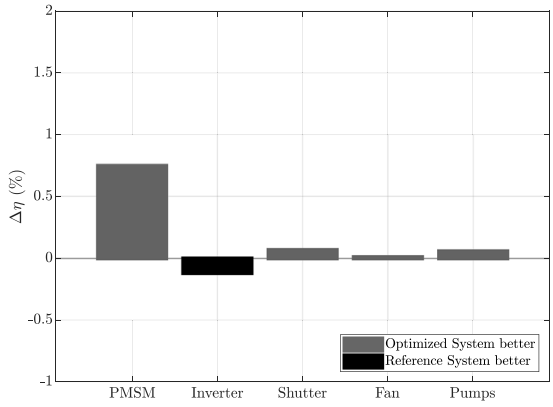

(b) Energy consumption impact of traction and actuator components for efficiency/performance rating of 1:0.01

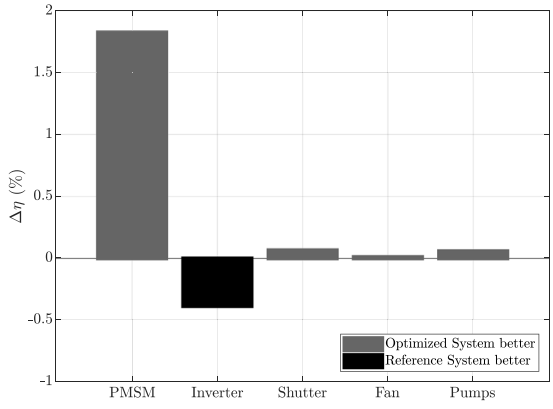

(c) Energy consumption impact of traction and actuator components for efficiency/performance rating of 1:0

Fig. 16. Comparison of HV energy consumption impact between RB baseline system and NMPC optimized system.

sum it up, in the selected use-cases the influence of the actuators is more or less neglectable, compared to the PMSM and inverter. In future contributions, extending this methodology, already mentioned worst-case and durability scenarios have to be added into the design process, to verify the system's feasibility with the implemented actuator capabilities under the harshest conditions.

The suspected opposing trends between inverter and PMSM from system one to three, cannot just be found from control strategy point of view, but also from power consumption. Starting with the inverter, the adjustments of the gear ratios from $10.65 \rightarrow 10.73 \rightarrow 10.36 \rightarrow 7.32$ have an immediate effect on the inverter losses $P_{\text{Loss,Inv}} = f(n, M, T_J, T_{\text{Wdg}})$, governing the trend from system one to three [8]. This negative trend is partly damped from the control strategy, keeping the junction temperature as low as possible, if it makes sense from overall system perspective, as has been seen for the highway use-case in Fig. 15(b).

Compared to the inverter the absolute PMSM efficiency trend dominates the systems influence. Accordingly, the PMSM efficiency rises from -0.55% over 0.74% to 1.83%. Responsible is on the one hand side the wider machine diameter, increasing the slot area and anti-proportionally decreasing wire resistance and DC-copper losses (see B.29). On the other hand, load point adjustments to lower speed and higher torque is reducing the frequency dependent iron losses successively, so that all loss components could be optimized in system design three.

5.5. System trend analysis

To extend the evaluation of the system interaction potential, a system trend analysis is carried out. With this predictive approach, using the posterior mean values of the trained GPs, trade-offs between design parameters and their influence on design objectives and controller outputs can be visualized. Therefore, 3D-slices of the multi-dimensional parameter space, crossing the reference parameter set, are created. The results of this method are shown for the objectives in Fig. 17 and in Fig. 18 for the control outputs, respectively. As no necessary fan actuation in the selected use-cases has been observed, a trend analysis is excluded in Fig. 18.

In the top row of Fig. 17 the total energy consumption prediction is depicted, reaching its minimum in a sweet spot with a gear ratio roughly below 10. For higher gear ratios the system efficiency decreases, because of increased frequency losses on EM and inverter side. The same trend exists when going to even lower gear ratios, where increased torque leads to higher conduction and copper losses. Second trend can be slightly encountered by increasing the diameter or reducing the length, as has happened in all three final designs. While reducing the gear ratio from the reference value helps lowering energy consumption, a clear performance pareto front is recognizable for a gear ratio again shortly below 10. Besides the velocity deviation in the city cycle at this configuration, climbing capabilities would also be affected, but have not been part of the first methodology implementation yet. Increasing EM torque output by maximizing PMSM length and diameter is the only possibility to lower the pareto front marginally. In further contributions a hard performance constraint on feasible system designs, for example as an outcome of a customer survey, shall be included in the BO process as an error model. A mitigation opportunity of the performance degradation in this work would be to introduce a switchable two-speed transmission to satisfy the trade-off between agility and energy consumption [65]. In terms of temperature trade-offs in the bottom row, the reference design is already close to the sweet spot of the lowest temperature progression, which is around a gear ratio of 10 and machines with maximized dimensions. The first observation results from the same worse operating point shifts as has been mentioned for the energy consumption trends. The second conclusion is simply because of the increased thermal mass in bigger machines. All in all no critical temperatures are observed, which highlight the need of a broader use-case coverage in future contributions.

The control outputs of the NMPC in Fig. 18 are showing a similar trend as the total energy consumption predictions. In the upper row, the pumps power consumption is visualized. Depending on the EM dimensions a minimum in pump speed is observed, when reducing the length and increasing the diameter at the same time. This trend is mainly governed from the electrical winding resistance trend in the

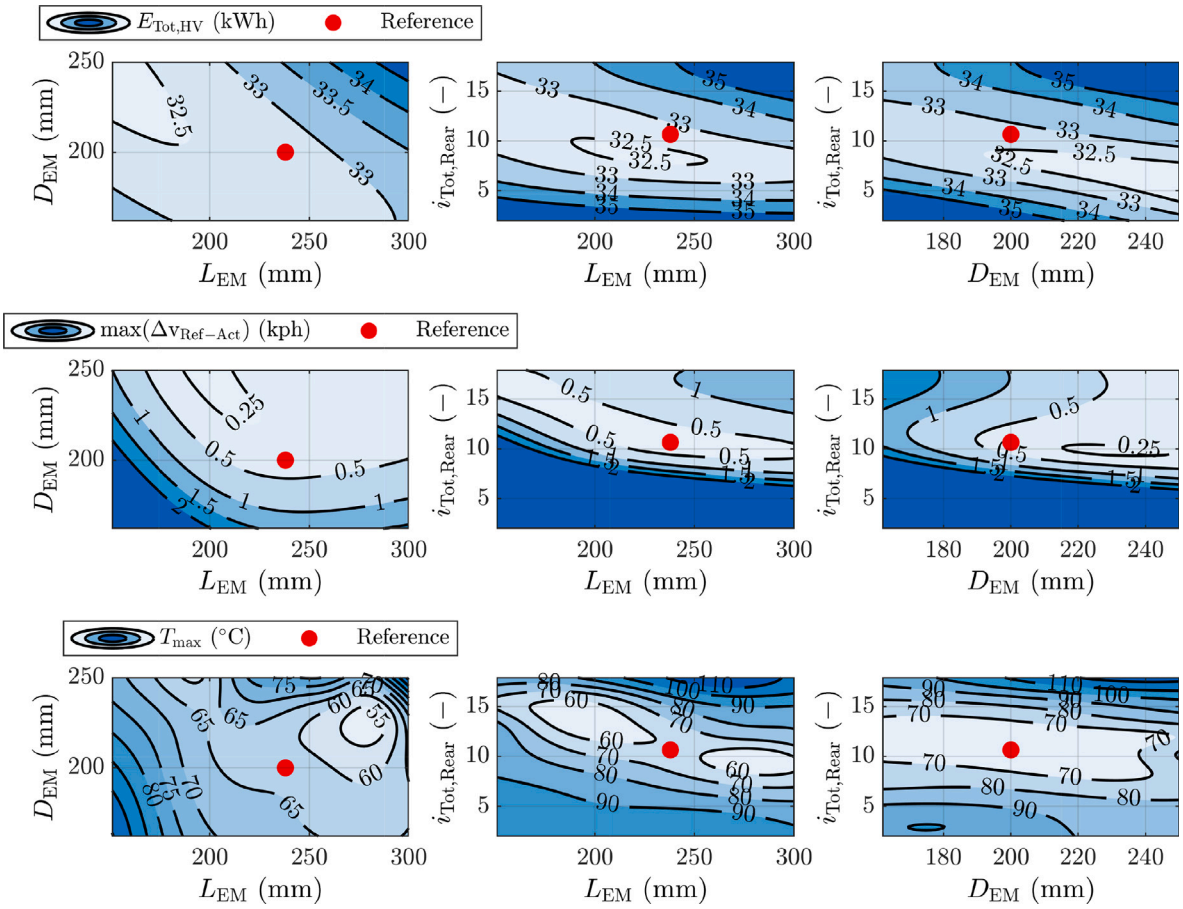

Fig. 17. Design objective trends for variation of PMSM length, diameter and total gear ratio.

stator slots. The more dominating trend to higher pump speeds, are machines with really small or big dimensions and high or low total gear ratios. First statement is underlining the "right-sizing" effect on the whole system requirements. A bigger machine would be operated at less efficiency in the selected use-cases, and higher thermal dissipation rates need to be considered, while secondly the inverter needs to provide more current in a smaller machine. This results in overall increased inverter losses. Second statement for the gear ratio trend undergoes the same argumentation as for the energy consumption, only that the effect is governed due to higher thermal requirements, when scattering higher or lower around the reference design. As mentioned for the pump cooling with smaller EM dimensions and low gear ratios, also the shutter opening is affected by increased inverter losses to dissipate heat to the ambient and bringing the inverter junction temperature down. Hence, the shutter power consumption could be decreased by increasing EM dimensions, especially the diameter and therewith rotor flux accordingly. Lastly, equivalent bypass opening time is shown in the bottom row of Fig. 18. It has already been pointed out, that bypass and shutter control are closely coupled, as they affect the lowest circuit temperature equally. Generally speaking, reduced EM dimensions and gear ratios, lead to more frequent openings of the bypass and shutter to create a precise mixture temperature. This ensures to maintain high EM magnet temperatures on the highway, while precisely cooling the inverter junction in acceleration phases. Looking at the whole picture and understanding the EM length reduction, the advantages of overall lower energy consumption, pump power consumption reduction and higher EM temperatures for thermal field weakening, outweigh the effect of increased shutter and bypass control to overcome inverter loss challenges with such machines. This finally underlines the need of a system perspective analysis, including control and design, in an EV development process.

6. Conclusion

In this contribution a novel methodology for an EM development process has been introduced, including a combination of electromagnetic design and online thermal system control optimization within a multi-layer nested framework. This approach ensures alignment with system objectives by integrating specific system use-cases and therewith emphasizing a "mission-specific" powertrain optimization strategy. The methodology leverages Bayesian Optimization (BO) and gradient-based Nonlinear Model Predictive Control (NMPC) algorithms, achieving a performance increase of 13% and energy consumption reduction of $-0.18\ \frac{\mathrm{kWh}}{100\ \mathrm{km}}$ at the same time regarding the derived reference system.

Two distinct objective functions were necessary for each optimization layer, addressing energy, performance and durability optimality criteria. For system evaluation purposes, an automatic system setup and design process has been established, ranging from the geometrical component candidate derivation, over the thermal and electromagnetic model building, till the NMPC compilation and system simulation. In the end, three parameter studies revealed critical trade-offs between efficiency and performance. A counteracting trend was observed in the EM and inverter characteristics, where reducing the final gear ratio led to increased EM efficiency by shifting load points, particularly those from the energy-intensive highway cycle, into high-efficiency regions,

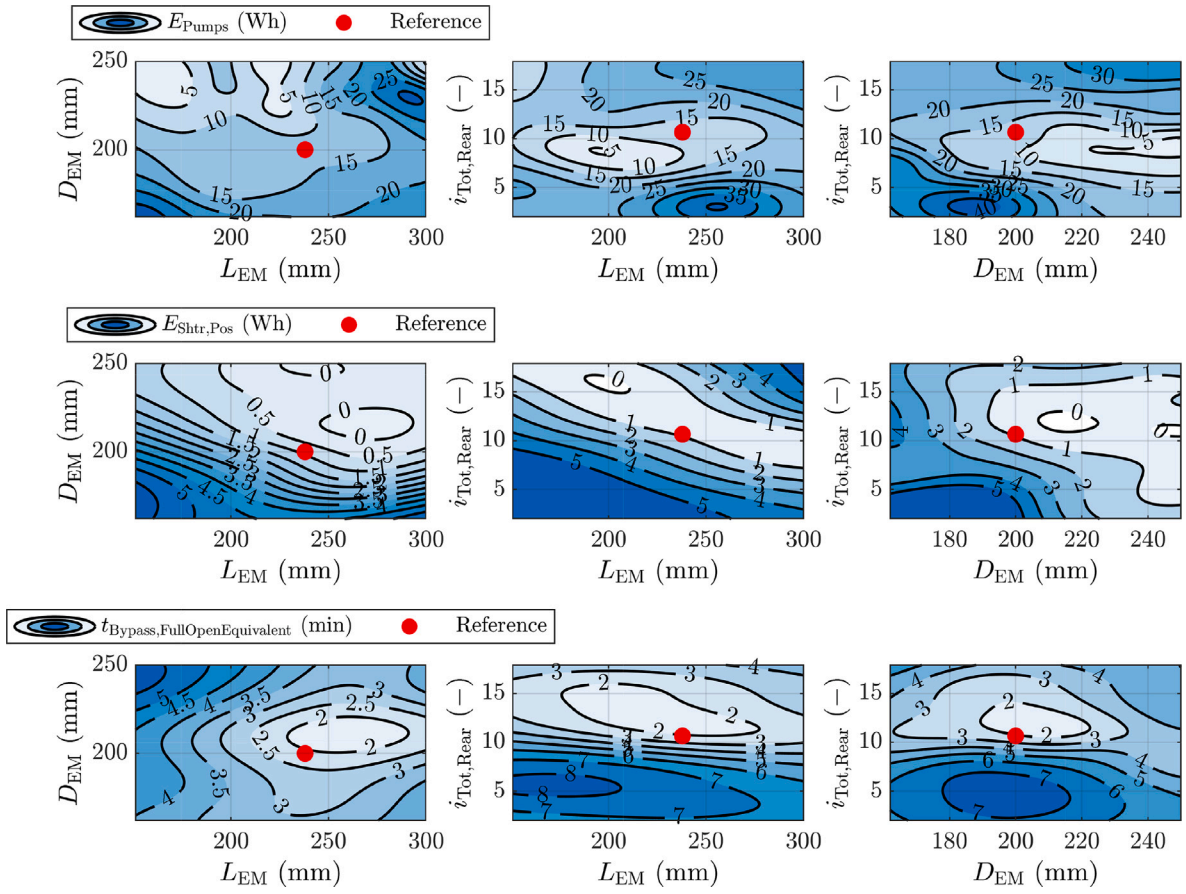

Fig. 18. NMPC control actuation trends for variation of PMSM length, diameter and total gear ratio.

while the inverter effectiveness decreased. This finding outlines the necessity of system impact analysis of each individual component design process, which is one key driver of the presented co-optimization framework. Control optimization and system adaptation were achieved across the city and highway cycles. Systems with lower PMSM base efficiency and higher heat losses demonstrated a preference for active temperature control, whereas systems with higher PMSM base efficiency exhibited reduced actuation frequency, focusing on minimizing inverter losses. These findings underscore the potential of integrating thermal and control aspects into an early system and component design stage. For further enhancements in future contributions, the design use-cases shall be expanded to include worst-case scenarios, such as elevated ambient temperatures or climbing conditions. Additionally, the framework could be extended to incorporate alternative EM configurations, powertrain architectures, and thermal system layouts, offering opportunities to further improve system performance and adaptability.

Finally, this study has revealed the potential benefits of integrating control and hardware design to enhance system performance and energy efficiency. However, the design parameter space still needs extension for an active learning of the cooling layout. Moreover, NVH and optimal motion control objectives have not been part of the process yet. Both enhancements of the problem formulation shall facilitate the generalizable character of this approach, but will increase the computational effort for the NMPC online system optimization. Here, a possible solution would be combining RL and NMPC to achieve a simultaneous imitation learning of the optimized controls for certain trajectories.

CRediT authorship contribution statement

Christoph Wellmann: Writing – review & editing, Writing – original draft, Software, Methodology, Formal analysis, Data curation, Conceptualization. **Abdul Rahman Khaleel:** Writing – original draft, Software, Methodology. **Tobias Brinkmann:** Writing – review & editing, Methodology. **Alexander Wahl:** Writing – review & editing, Methodology. **Christian Monissen:** Writing – review & editing, Data curation. **Markus Eisenbarth:** Writing – review & editing, Supervision. **Jakob Andert:** Writing – review & editing, Writing – original draft, Supervision.

Declaration of competing interest

The authors declare that they have no known competing financial interests or personal relationships that could have appeared to influence the work reported in this paper.

Acknowledgment

This paper was partially created in the context of the ESCALATE project. The project has received funding from the European Climate, Infrastructure and Environment Executive Agency (CINEA), Belgium under grant agreement No 101096598. This publication reflects only the author' s view. The Agency is not responsible for any use that may be made of the information it contains.
Images used courtesy of ANSYS, Inc.

Appendix A. Component model validation

See Figs. A.19–A.24.

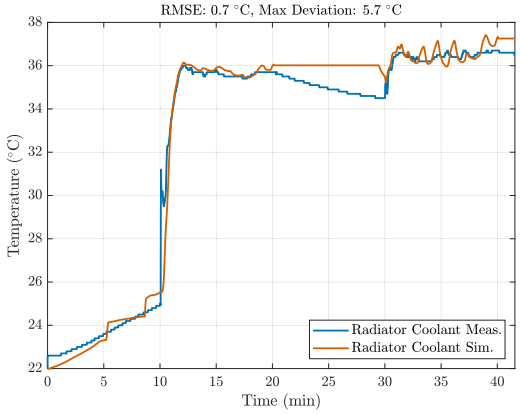

Fig. A.19. Comparison of the radiator coolant outlet temperature: SC03 test bench measurement vs. component model simulation.

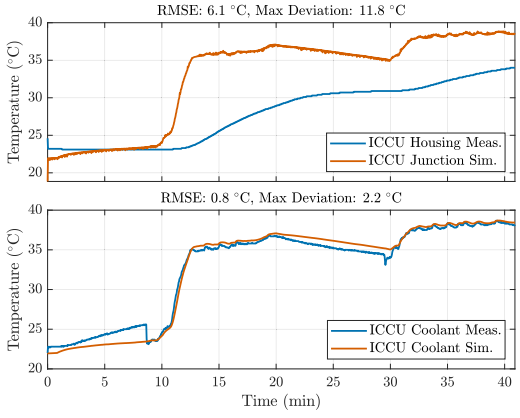

Fig. A.20. Comparison of the ICCU junction/housing and coolant outlet temperatures: SC03 test bench measurement vs. component model simulation.

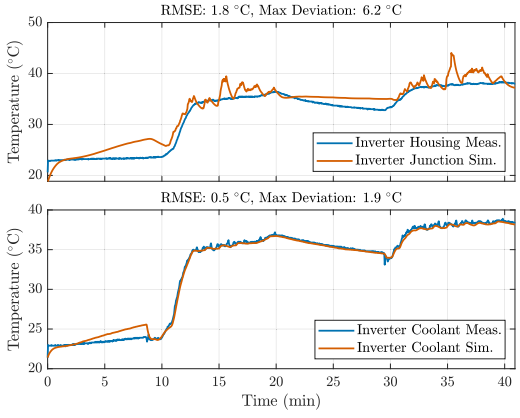

Fig. A.21. Comparison of the inverter junction/housing and coolant outlet temperatures: SC03 test bench measurement vs. component model simulation.

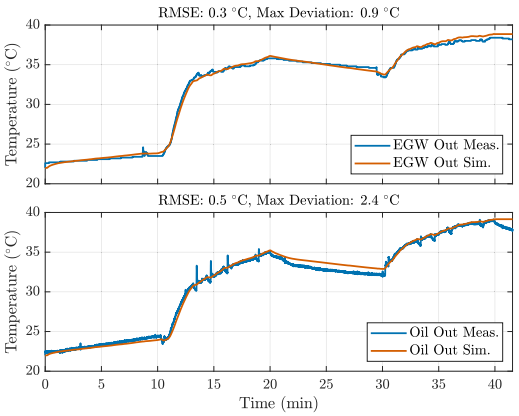

Fig. A.22. Comparison of the 4-way HEX water-glycol and oil outlet temperatures: SC03 test bench measurement vs. component model simulation.

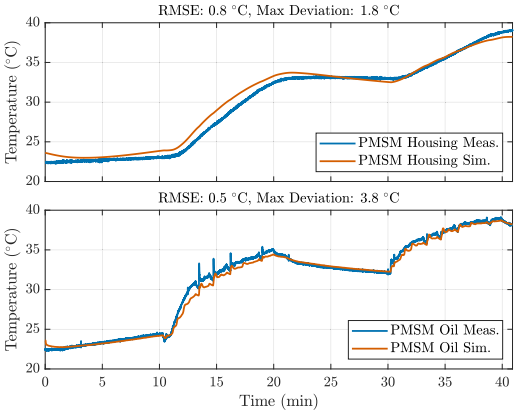

Fig. A.23. Comparison of the PMSM housing and merged spray/shaft cooling outlet temperatures: SC03 test bench measurement vs. component model simulation.

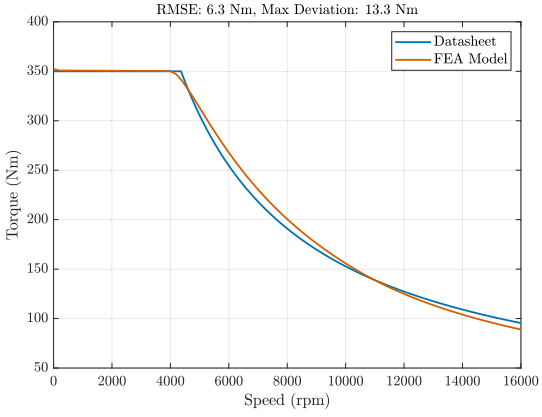

Fig. A.24. Peak torque characteristic validation of rear PMSM FEA model against manufacturer data.

Appendix B. Extended results

See Figs. B.25–B.29.

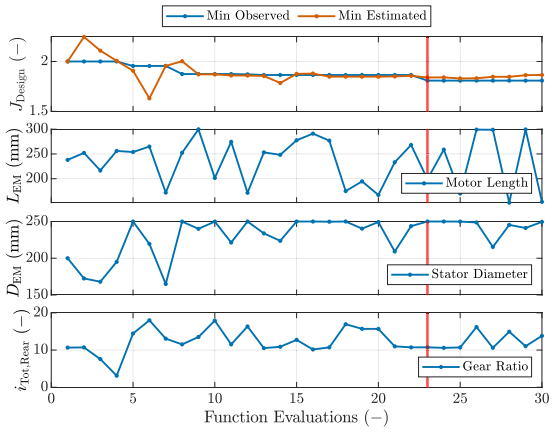

(a) Length, diameter and gear ratio variations with GP minimum estimation for efficiency/performance rating of 1:1

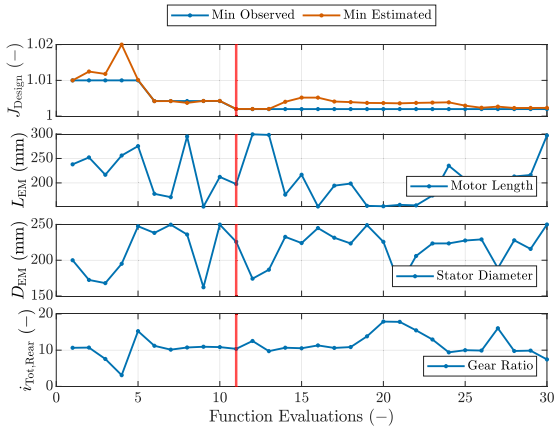

(b) Length, diameter and gear ratio variations with GP minimum estimation for efficiency/performance rating of 1:0.01

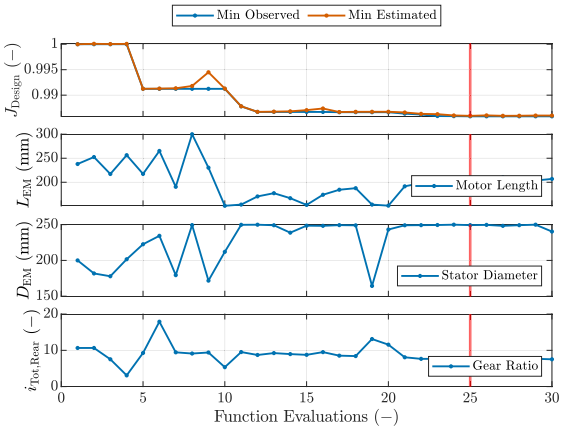

(c) Length, diameter and gear ratio variations with GP minimum estimation for efficiency/performance rating of 1:0

Fig. B.25. Observation parameter trace during Bayesian Optimization algorithm.

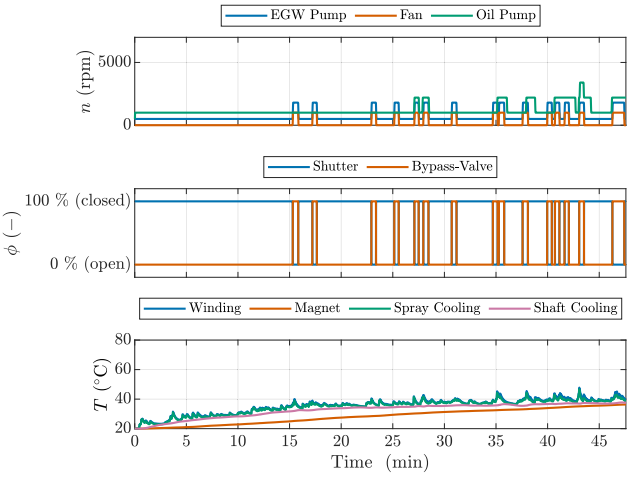

(a) System controls and PMSM temperatures city use-case

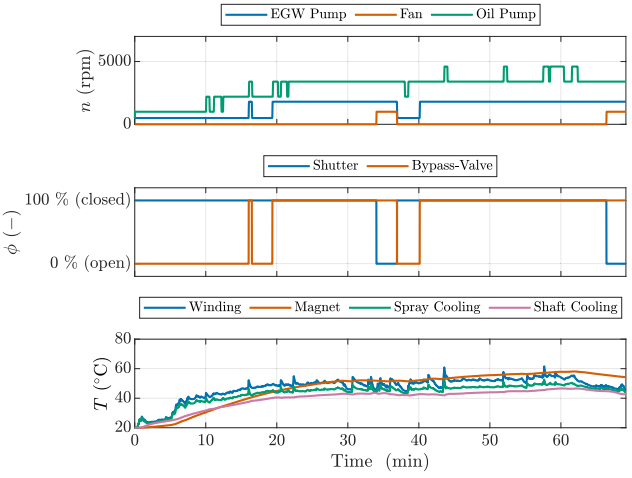

(b) System controls and PMSM temperatures highway use-case

Fig. B.26. Transient control and temperatures of referenced system with rule-based control strategy.

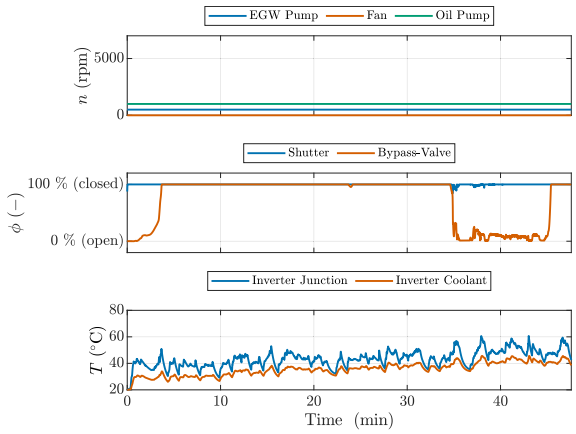

(a) System controls and inverter temperatures for efficiency/performance rating of 1:1

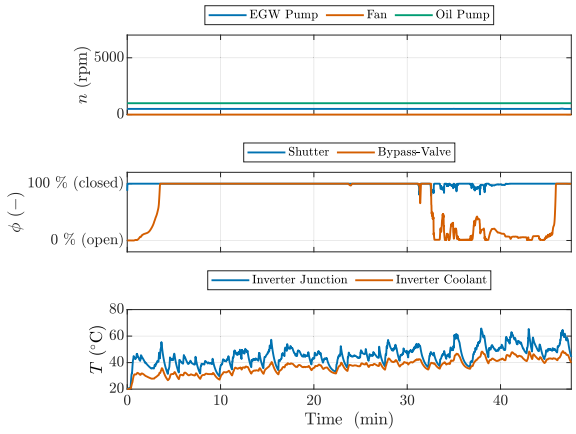

(b) System controls and inverter temperatures for efficiency/performance rating of 1:0.01

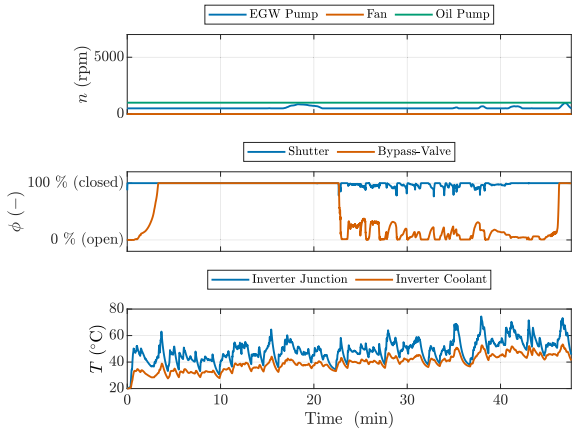

(c) System controls and inverter temperatures for efficiency/performance rating of 1:0

Fig. B.27. Transient system controls in city use-case at $T_{\text{Amb}} = 20\,°\text{C}$, focusing inverter influence.

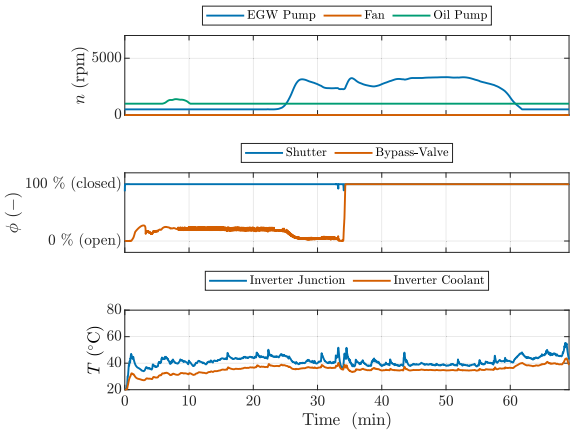

(a) System controls and inverter temperatures for efficiency/performance rating of 1:1

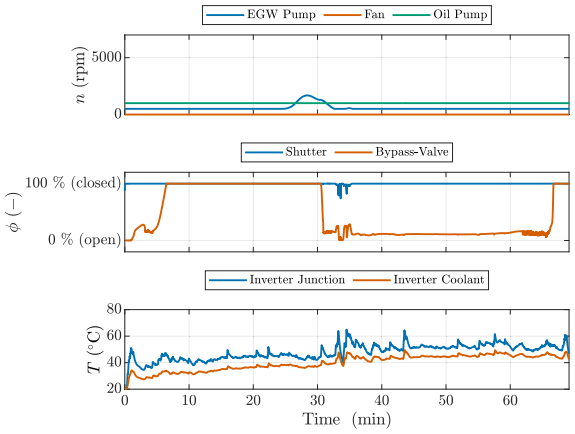

(b) System controls and inverter temperatures for efficiency/performance rating of 1:0.01

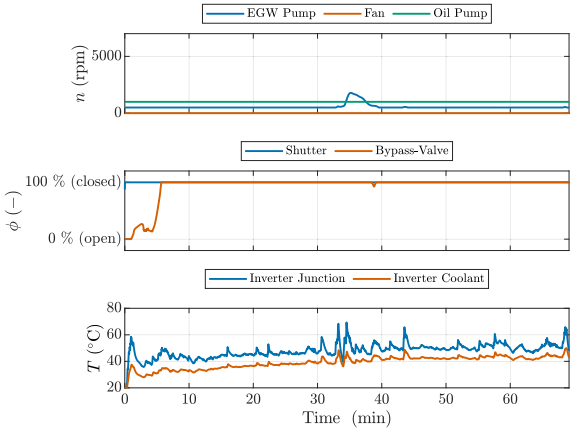

(c) System controls and inverter temperatures for efficiency/performance rating of 1:0

Fig. B.28. Transient system controls in highway use-case at $T_{\text{Amb}} = 20\,°\text{C}$, focusing inverter influence.

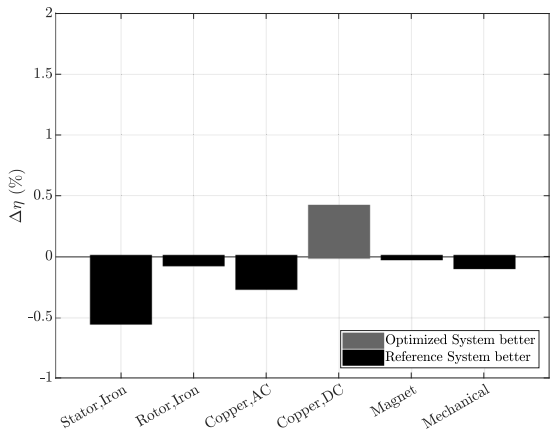

(a) Iron, copper and mechanical loss decrease of optimized PMSM for efficiency/performance rating of 1:1

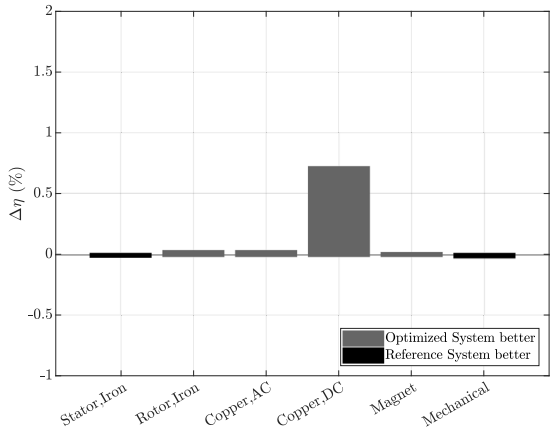

(b) Iron, copper and mechanical loss decrease of optimized PMSM for efficiency/performance rating of 1:0.01

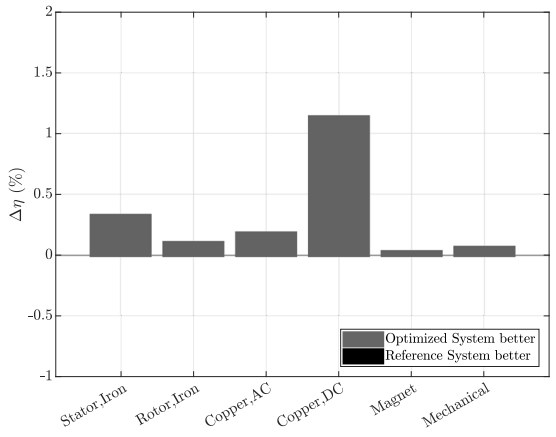

(c) Iron, copper and mechanical loss decrease of optimized PMSM for efficiency/performance rating of 1:0

Fig. B.29. Comparison of PMSM loss effects between baseline and optimized system for three different design objective weightings.

Data availability

Data will be made available on request.

References

[1] International Energy Agency. Global EV outlook. 2024, URL https://www.iea.org/reports/global-ev-outlook-2024. (Accessed 22 October 2024).

[2] International Energy Agency. Global energy outlook. 2023, URL https://www.iea.org/reports/world-energy-outlook-2023. (Accessed 22 October 2024).

[3] Razmjoo A, Ghazanfari A, Jahangiri M, Franklin E, Denai M, Marzband M, Astiaso Garcia D, Maheri A. A comprehensive study on the expansion of electric vehicles in Europe. Appl Sci 2022. http://dx.doi.org/10.3390/app122211656.

[4] Acar E, Jain N, Ramu P, Hwang C, Lee I. A survey on design optimization of battery electric vehicle components, systems, and management. Struct Multidiscip Optim 2024. http://dx.doi.org/10.1007/s00158-024-03737-7.

[5] Roshandel E, Mahmoudi A, Kahourzade S, Yazdani A, Shafiullah GM. Losses in efficiency maps of electric vehicles: An overview. Energies 2021. http://dx.doi.org/10.3390/en14227805.

[6] Dan D, Zhao Y, Wei M, Wang X. Review of thermal management technology for electric vehicles. Energies 2023. http://dx.doi.org/10.3390/en16124693.

[7] He L, Jing H, Zhang Y, Li P, Gu Z. Review of thermal management system for battery electric vehicle. J Energy Storage 2023. http://dx.doi.org/10.1016/j.est.2022.106443.

[8] Wahl A, Wellmann C, Krautwig B, Manns P, Chen B, Schernus C, Andert J. Efficiency increase through model predictive thermal control of electric vehicle powertrains. Energies 2022. http://dx.doi.org/10.3390/en15041476.

[9] Wahl A, Wellmann C, Monissen C, Andert J. Active temperature control of electric drivetrains for efficiency increase. Appl Energy 2023. http://dx.doi.org/10.1016/j.apenergy.2023.120887.

[10] Wallscheid O, Bocker J. Derating of automotive drive systems using model predictive control. In: IEEE international symposium on predictive control of electrical drives and power electronics. PRECEDE, 2017, http://dx.doi.org/10.1109/PRECEDE.2017.8071264.

[11] Winkler A, Frey J, Fahrbach T, Frison G, Scheer R, Diehl M, Andert J. Embedded real-time nonlinear model predictive control for the thermal torque derating of an electric vehicle. IFAC-PapersOnLine 2021. http://dx.doi.org/10.1016/j.ifacol.2021.08.570.

[12] Monissen C, Kusche O, Schröder M, Andert J. Power density increase in permanent-magnet synchronous machines considering active thermal control. Energies 2023. http://dx.doi.org/10.3390/en16217369.

[13] Clemente M, Salazar M, Hofman T. Concurrent design optimization of powertrain component modules in a family of electric vehicles. 2023, http://dx.doi.org/10.48550/arXiv.2311.03167, arXiv.

[14] Wei C. Optimal design and control of electrified powertrains (Ph.D. thesis), Netherlands: Technische Universiteit Eindhoven; 2020.

[15] Azad S, Alexander-Ramos MJ. Robust combined design and control optimization of hybrid-electric vehicles using MDSDO. IEEE Trans Veh Technol 2021. http://dx.doi.org/10.1109/TVT.2021.3071863.

[16] Verbruggen F, Salazar M, Pavone M, Hofman T. Joint design and control of electric vehicle propulsion systems. In: IEEE European control conference. ECC, 2020, http://dx.doi.org/10.23919/ECC51009.2020.9143869.

[17] Haskara I, Hegde B, Chang C-F. Reinforcement learning based EV energy management for integrated traction and cabin thermal management considering battery aging. IFAC-PapersOnLine 2022. http://dx.doi.org/10.1016/j.ifacol.2022.10.308.

[18] Choi W, Kim JW, Ahn C, Gim J. Reinforcement learning-based controller for thermal management system of electric vehicles. In: IEEE vehicle power and propulsion conference. VPPC, 2022, http://dx.doi.org/10.1109/VPPC55846.2022.10003470.

[19] Wang X, Wang R, Shu G, Tian H, Zhang X. Energy management strategy for hybrid electric vehicle integrated with waste heat recovery system based on deep reinforcement learning. Sci China Technol Sci 2022. http://dx.doi.org/10.1007/s11431-021-1921-0.

[20] Borsboom O, Lokker M, Salazar M, Hofman T. Effective scaling of high-fidelity electric motor models for electric powertrain design optimization. 2023, http://dx.doi.org/10.48550/arXiv.2307.12741, arXiv.

[21] Ban B, Stipetic S. Design and optimization of synchronous reluctance machine for actuation of electric multi-purpose vehicle power take-off. In: IEEE international conference on electrical machines. ICEM, 2020, http://dx.doi.org/10.1109/ICEM49940.2020.9270784.

[22] Ban B, Kersten A, Andersson A, Stipetic S. Metamodel-based design and optimization of a spoke-type interior permanent magnet machine for a vehicle traction application. In: IEEE XIV international symposium on industrial electronics and applications. INDEL, 2022, http://dx.doi.org/10.1109/INDEL55690.2022.9965493.

[23] You Y-m. Multi-objective optimal design of permanent magnet synchronous motor for electric vehicle based on deep learning. Appl Sci 2020. http://dx.doi.org/10.3390/app10020482.

[24] Schönknecht A, Babik A, Rill V. Electric powertrain system design of BEV and HEV applying a multi objective optimization methodology. Transp Res Procedia 2016. http://dx.doi.org/10.1016/j.trpro.2016.05.429.

[25] Mutluer M, Bilgin O. Design optimization of PMSM by particle swarm optimization and genetic algorithm. In: IEEE international symposium on innovations in intelligent systems and applications. 2012, http://dx.doi.org/10.1109/INISTA.2012.6247024.

[26] Zhang S, Li S, Harley RG, Habetler TG. An efficient multi-objective Bayesian optimization approach for the automated analytical design of switched reluctance machines. In: 2018 IEEE energy conversion congress and exposition. ECCE, 2018, http://dx.doi.org/10.1109/ECCE.2018.8557480.

[27] Fang L-c, Qin S-y. Concurrent optimization for parameters of powertrain and control system of hybrid electric vehicle based on multi-objective genetic algorithms. In: IEEE SICE-ICASE international joint conference. 2006, http://dx.doi.org/10.1109/SICE.2006.315114.

[28] Yang N, Ruan S, Han L, Liu H, Guo L, Xiang C. Reinforcement learning-based real-time intelligent energy management for hybrid electric vehicles in a model predictive control framework. Energy 2023. http://dx.doi.org/10.1016/j.energy.2023.126971.

[29] Sun X, Fu J, Yang H, Xie M, Liu J. An energy management strategy for plug-in hybrid electric vehicles based on deep learning and improved model predictive control. Energy 2023. http://dx.doi.org/10.1016/j.energy.2023.126772.

[30] Oh Y-H, Chung T-K, Kim M-K, Jung H-K. Optimal design of electric machine using genetic algorithms coupled with direct method. IEEE Trans Magn 1999. http://dx.doi.org/10.1109/20.767366.

[31] Lei N, Zhang H, Wang H, Wang Z. An improved co-optimization of component sizing and energy management for hybrid powertrains interacting with high-fidelity model. IEEE Trans Veh Technol 2023. http://dx.doi.org/10.1109/TVT.2023.3296114.

[32] Lin Y, McPhee J, Azad NL. Comparison of deep reinforcement learning and model predictive control for adaptive cruise control. IEEE Trans Intell Veh 2021. http://dx.doi.org/10.1109/TIV.2020.3012947.

[33] Norouzi A, Heidarifar H, Borhan H, Shahbakhti M, Koch CR. Integrating machine learning and model predictive control for automotive applications: A review and future directions. Eng Appl Artif Intell 2023. http://dx.doi.org/10.1016/j.engappai.2023.105878.

[34] Lei G, Zhu J, Guo Y, Liu C, Ma B. A review of design optimization methods for electrical machines. Energies 2017. http://dx.doi.org/10.3390/en10121962.

[35] Kamper MJ, van der Merwe FS, Williamson S. Direct finite element design optimisation of the cageless reluctance synchronous machine. IEEE Trans Energy Convers 1996. http://dx.doi.org/10.1109/60.537006.

[36] Garnett R. Bayesian optimization. Cambridge University Press; 2023, http://dx.doi.org/10.1017/9781108348973.

[37] Herber DR, Allison JT. Nested and simultaneous solution strategies for general combined plant and control design problems. J Mech Des 2019. http://dx.doi.org/10.1115/1.4040705.

[38] FEV Global Benchmarking. Hyundai IONIQ 5 drivetrain testing: thermal management. Internal report, FEV Consulting; 2023, Confidential.

[39] FEV Global Benchmarking. Hyundai IONIQ 5 drivetrain tier-down: PMSM layout. Internal report, FEV Consulting; 2022, Confidential.

[40] Ansys®, Motor-CAD R2. 2023, URL https://www.ansys.com/products/electronics/ansys-motor-cad. (Accessed 22 October 2024).

[41] Stipetic S, Goss J, Zarko D, Popescu M. Calculation of efficiency maps using a scalable saturated model of synchronous permanent magnet machines. IEEE Trans Ind Appl 2018. http://dx.doi.org/10.1109/TIA.2018.2837672.

[42] Aroua A, Lhomme W, Verbelen F, Ibrahim MN, Bouscayrol A, Sergeant P, Stockman K. Impact of scaling laws of permanent magnet synchronous machines on the accuracy of energy consumption computation of electric vehicles. eTransportation 2023. http://dx.doi.org/10.1016/j.etran.2023.100269.

[43] Deng J, Bae C, Denlinger A, Miller T. Electric vehicles batteries: Requirements and challenges. Joule 2020. http://dx.doi.org/10.1016/j.joule.2020.01.013.

[44] Schueppel F, Schlüter M, Braunschweig J. Design of battery electric vehicles in accordance with legal standards and manufacturers' and customers' requirements. In: Der Antrieb von morgen 2017. 2017, http://dx.doi.org/10.13140/RG.2.2.27956.96642.

[45] Denis N, Odawara S, Fujisaki K. Attempt to evaluate the building factor of a stator core in inverter-fed permanent magnet synchronous motor. IEEE Trans Ind Electron 2017. http://dx.doi.org/10.1109/TIE.2016.2573267.

[46] Chattejee D, Chakraborty C, Dalapati S. Pulse-width modulation techniques in two-level voltage source inverters – state of the art and future perspectives. Power Electron Drives 2023. http://dx.doi.org/10.2478/pead-2023-0023.

[47] Prof Dr Uwe Scheuermann. AN1501: Estimation of liquid cooled heat sink performance at different operation conditions. 2015, URL https://www.semikron-danfoss.com/service-support/downloads.html. (Accessed 22 October 2024).

[48] Chen B, Wulff C, Etzold K, Manns P, Birmes G, Andert J, Pischinger S. A comprehensive thermal model for system-level electric drivetrain simulation with respect to heat exchange between components. In: IEEE intersociety conference on thermal and thermomechanical phenomena in electronic systems. ITherm, 2020, http://dx.doi.org/10.1109/ITherm45881.2020.9190448.

[49] Wallscheid O, Bocker J. Global identification of a low-order lumped-parameter thermal network for permanent magnet synchronous motors. IEEE Trans Energy Convers 2016. http://dx.doi.org/10.1109/TEC.2015.2473673.

[50] MathWorks. Curve fitting toolbox: User's guide. 2023, URL https://de.mathworks.com/products/curvefitting.html. (Accessed 22 October 2024).

[51] Verschueren R, Frison G, Kouzoupis D, Frey J, van Duijkeren N, Zanelli A, Novoselnik B, Albin T, Quirynen R, Diehl M. Acados—a modular open-source framework for fast embedded optimal control. Math Program Comput 2022. http://dx.doi.org/10.1007/s12532-021-00208-8.

[52] Nurkanović A, Zanelli A, Albrecht S, Frison G, Diehl M. Contraction properties of the advanced step real-time iteration for NMPC. IFAC-PapersOnLine 2020. http://dx.doi.org/10.1016/j.ifacol.2020.12.449.

[53] Bock HG, Plitt KJ. A multiple shooting algorithm for direct solution of optimal control problems *. IFAC Proc Vol 1984. http://dx.doi.org/10.1016/S1474-6670(17)61205-9.

[54] Frison G, Diehl M. HPIPM: a high-performance quadratic programming framework for model predictive control. IFAC-PapersOnLine 2020. http://dx.doi.org/10.1016/j.ifacol.2020.12.073.

[55] Ljung L. System identification toolbox: User's guide. 2008, URL https://www.lehigh.edu/~eus204/teaching/ME450_SIRC/matlab/MAT_ident.pdf. (Accessed 22 October 2024).

[56] Hemmati S, Doshi N, Hanover D, Morgan C, Shahbakhti M. Integrated cabin heating and powertrain thermal energy management for a connected hybrid electric vehicle. Appl Energy 2021. http://dx.doi.org/10.1016/j.apenergy.2020.116353.

[57] Shah RK, Sekulić DP. Fundamentals of heat exchanger design. Wiley; 2003, http://dx.doi.org/10.1002/9780470172605.

[58] MathWorks. MATLAB - statistics and machine learning toolbox. 2023, URL https://www.mathworks.com/products/statistics.html. (Accessed 22 October 2024).

[59] Bickel P, Diggle P, Fienberg S, Krickeberg K, Olkin I, Wermuth N, Zeger S, Neal RM. Bayesian learning for neural networks. Springer New York; 1996, http://dx.doi.org/10.1007/978-1-4612-0745-0.

[60] Snoek J, Larochelle H, Adams RP. Practical Bayesian optimization of machine learning algorithms. 2012, http://dx.doi.org/10.48550/arXiv.1206.2944, arXiv.

[61] Rasmussen CE, Williams CKI. Gaussian processes for machine learning. Adaptive computation and machine learning, The MIT Press; 2006, http://dx.doi.org/10.7551/mitpress/3206.001.0001.

[62] Frazier PI. A tutorial on Bayesian optimization. 2018, http://dx.doi.org/10.48550/arXiv.1807.02811, arXiv.

[63] Bauer D. Verlustanalyse bei elektrischen Maschinen für Elektro- und Hybridfahrzeuge zur Weiterverarbeitung in thermischen Netzwerkmodellen. Springer Fachmedien Wiesbaden; 2019, http://dx.doi.org/10.1007/978-3-658-24272-5.

[64] Yang J, Che Y, Ran L, Jiang H. Evaluation of frequency and temperature dependence of power losses difference in parallel IGBTs. IEEE Access 2020. http://dx.doi.org/10.1109/ACCESS.2020.2995971.

[65] Dr Ing, AG HCFP. The technology behind the new porsche taycan. 2024, URL https://newsroom.porsche.com/dam/jcr:93483663-c12b-43ca-98f5-b1b8b845e321/PAG_Taycan_Technology_PM_EN.pdf.PDF. (Accessed 22 October 2024).